COLORADO
Department of Transportation

Applied Research and Innovation Branch

Caisson Drilling Fluid Interaction with Fine Grained Bedrock

Authors

Mitul Sisodiya
Shubjot Singh
Yida Zhang, Ph.D.
Ronald Pak, Ph.D.

Report No. CDOT-2020-04
February 2020

The contents of this report reflect the views of the authors, who are responsible for the facts and accuracy of the data presented herein. The contents do not necessarily reflect the official views of the Colorado Department of Transportation or the Federal Highway Administration. This report does not constitute a standard, specification, or regulation

Technical Report Documentation Page

1. Report No.	2. Government Accession No.	3. Recipient's Catalog No.
CDOT-2020-04		

4. Title and Subtitle	5. Report Date
Caisson Drilling Fluid Interaction with Fine Grained Bedrock	February 2020
	6. Performing Organization Code

7. Author(s)	8. Performing Organization Report No.
Mitul Sisodiya, Shubjot Singh, Yida Zhang, Ronald Y.S. Pak	

9. Performing Organization Name and Address	10. Work Unit No. (TRAIS)
Department of Civil, Environmental & Architectural Engineering University of Colorado Boulder, CO 80309-0428	
	11. Contract or Grant No. 218.03

12. Sponsoring Agency Name and Address	13. Type of Report and Period Covered
Colorado Department of Transportation - Research 2829 W. Howard Pl. Denver CO, 80204	Final
	14. Sponsoring Agency Code

15. Supplementary Notes
Prepared in cooperation with the US Department of Transportation, Federal Highway Administration

16. Abstract
This report presents a comprehensive evaluation on the effect of drilling fluid infiltration in claystone bedrock on the axial capacity of drilled caissons. The methodology of this research combines experimental testing and numerical simulations. The results obtained in the experimental phase are used to inform the numerical study. In the experimental phase, extensive laboratory experiments are conducted on claystone samples from three sites near Denver; I-70 & Colfax, I-70 & Wadsworth and C-470 & Wads (referred as site-1, 2 and 3 hereafter) to quantify the abovementioned hydro-mechanical interactions. In the second phase, Finite Element Analyses (FEA) on drilled caisson has been performed to quantify the bearing capacity reduction due to excessive wetting of the bedrock. It is predicted that for all three sites with various permeability and strength reduction characteristics, the pile capacity reduction for 4-hour wetting is less than 15%, despite several very conservative assumptions adopted in the study**.** It is therefore concluded that the 4-hour limitation is quite reasonable and perhaps on the conservative side for the construction of drilled caissons.

17. Keywords	18. Distribution Statement
Denver Blue claystone, Shear strength, Water retention, Fluid weakening, Slaking, Pile axial capacity, Finite element method, ABAQUS	This document is available on CDOT's website http://www.coloradodot.info/programs/research/pdfs

19. Security Classif. (of this report)	20. Security Classif. (of this page)	21. No. of Pages	22. Price
Unclassified	Unclassified		

Form DOT F 1700.7 (8-72) Reproduction of completed page authorized

Final Project Report for Research Project 218.03

Caisson Drilling Fluid Interaction with Fine Grained Bedrock

by

Mitul Sisodiya

Shubjot Singh

Yida Zhang, Ph.D.

Ronald Y.S. Pak, Ph.D.

Department of Civil, Environmental & Architectural Engineering
University of Colorado Boulder
CO 80309-0428

February 2020

CDOT PROJECT COORDINATOR: **Amanullah Mommandi, P.E.**

CDOT TECHNICAL PANEL LEADER: **David Thomas, Ph.D., P.E.**

ACKNOWLEDGEMENTS

The authors like to thank CDOT's DTD Applied Research and Innovation Branch for funding and support of this study. The Study Panel includes David Thomas, Andy Pott, Trever Wang, Teddy Meshesha, David Vara, and Dustin Robbins. Their input and suggestions throughout the project are gratefully acknowledged.

EXECUTIVE SUMMARY

This report presents the results form a research project to evaluate the effects of drilling fluid infiltration in claystone bedrock on the axial load bearing capacity of drilled caissons in the Denver area. The methodology of this research combines laboratory soil testing and finite element simulations. In the first stage of this study, we performed extensive laboratory experiments to quantify the shear strength variation at different water saturation and the hydraulic characteristics of the claystone samples obtained from three different sites near Denver: I-70 & Colfax, I-70 & Wadsworth and C-470 & Wads. To evaluate the reduction in ultimate axial load capacity for different wetting times, extensive numerical simulations of drilled caissons were conducted through elastoplastic finite element analysis. Adopting the coupled unsaturated flow and mechanical analysis module provided by the commercial code ABAQUS, a versatile numerical simulation framework is developed for modeling the full process of drilling, fluid wetting, caisson construction, and in-situ axial loading. The material parameters obtained from the experimental phase are used to calibrate the material model in numerical simulation. The saturation-dependent shear strength parameters are introduced using a user-defined subroutine USFIELD developed in this project. It is predicted that for all three sites with various permeability and strength reduction characteristics, the pile capacity reduction for 4-hour wetting is less than 15%, despite several very conservative assumptions adopted in the study. It is therefore concluded that the 4-hour limitation is quite reasonable and perhaps on the conservative side for these sites. In addition to the site-specific simulations, parametric studies are conducted to isolate the effect of hydraulic conductivity and initial saturation of the in-situ claystone on the axial capacity reduction curves. These studies show that highly weathered or fissured claystone with low in-situ saturation can experience rapid and significant strength reduction upon wetting. Thus for this situation the constructor should limit the wetting time as much as possible. Future studies are needed to remove some of the conservative assumptions in this study and to investigate the capacity reduction if polymer fluid or slurry is used during drilling instead of water.

TABLE OF CONTENTS

LIST OF FIGURES

LIST OF TABLES

1. INTRODUCTION

A significant number of bridges and structures in Colorado are supported by drilled caisson and shafts embedded in weak fine-grained rocks such as Denver Blue Claystone and Pierre Shale. The construction and installation process of caisson inevitably involves some time lapse between the drilling of the shaft and subsequent placement of concrete. During this time (called wetting time hereafter), drilling fluid can infiltrate the bedrock and cause slaking and subsequent deterioration of the fine-grained claystone or shale rock mass. To safeguard against such adverse effects of drilling fluid-bedrock interactions, CDOT has stipulated a maximum four hours limit between the completion of drilling and the placement of concrete in the Drill Caisson Specification 503. The motivation behind this requirement is to limit the interaction between drilling fluid and bedrock. However, no systematic laboratory or field-scale studies were used to arrive at the four-hour time limit beyond their engineering judgement. The true time limit to avoid excessive degradation can be highly dependent on site-specific conditions, such as the water-sensitivity of the rock, the degree of fissuring and the in-situ degree of saturation. The objective of this study is to fill this knowledge gap and provide some references to determine the maximum allowable time between the drilling and the placement of concrete depending on the local site conditions. Considering that water has a stronger slaking and strength reduction effect on clay-bearing rocks than polymer- or slurry- based drilling fluids (Hemphill et al., 2008; Karakul, 2018), the investigation is limited to an evaluation of water-induced degradation in this pilot study.

The study is conducted in two phases: experimental phase and numerical phase. The results obtained in the experimental phase are used to inform the numerical study. For a given caisson geometry and depth, in a typical caisson design, the caisson axial bearing capacity depends on: 1) the intrinsic shear strength of the intact rock, 2) the variation of the strengths of intact rock and concrete-rock interface subjected to wetting, and 3) the hydraulic properties and the water retention characteristics of the intact rock. In the first phase of this study, a set of laboratory experiments are designed and conducted on claystone samples from three different Denver sites; I-70 & Colfax, I-70 & Wadsworth and C-470 & Wads (refereed as site-1, 2 and 3 hereafter) to quantify the abovementioned hydro-mechanical characteristics. In the second phase, finite element analysis (FEA) on drilled caisson are performed to quantify the bearing capacity reduction due to excessive

wetting of the bedrock. The experimental work is explained in section 2 of the report and the simulation work is explained in section 3

2. EXPERIMENTAL INVESTIGATION

2.1 Overview

The locations of the three sites and some pictures from drilling at site-1 are shown in Figure 1. The depths of the claystone samples are listed in Table 1. In the testing program, samples from each site are divided into two groups depending on the depth: those extracted from above the middle depth are labeled as "shallow" and below the middle depth are labeled as "deep". The depths corresponding to the shallow and deep samples are listed in Table 1 as well.

Table 1. Borehole and sample data

Site	Borehole depth	Shallow samples	Deep samples	Total length
1	$39'0" - 70'6"$	$39'0" - 54'9"$	$54'9" - 70'6"$	$31'6"$
2	$26'1" - 48'3"$	$26'1" - 37'2"$	$37'2" - 48'3"$	$22'2"$
3	$16'0" - 84'3"$	$16'0" - 50'1"$	$50'1" - 84'3"$	$68'3"$

The goal of this experimental program is to quantify the hydraulic properties of Denver Blue Claystone obtained from these sites and their strength variation with respect to saturation. To achieve this, experimental protocols and devices are developed for : 1) preparation of uniformly unsaturated samples at different degree of saturations for direct shear tests and for soil water retention curve (SWRC) data points at high suction range, 2) Tempe cell test for SWRC data at low suction range, 3) direct shear tests to determine the peak and residual shear strength of variably saturated samples, and 4) flex-wall permeameter tests to determine the saturated hydraulic conductivity. The dry unit weight, natural water content, and index properties of crushed claystone are also measured and are reported in Table 2. Direct shear tests for the concrete-rock interface were also attempted but later abandoned for reasons explained in section 2.5.

Table 2. Index properties of clayey fraction, unit weight and water content of the undisturbed specimens

Site	LL (%)	PI (%)	w_n (%)	γ_d (kN/m^3)	γ_{sat} (kN/m^3)
1	67.3-75.3	14.1-39.3	28-36	13.6-15.2	19.2-30.6
2	32.8-44.1	6.7-13.1	13-18	17.4-20.2	20.1-27.4
3	29.7-48.7	1.9-23.6	10-15	16.7-18.3	21.6-23.74

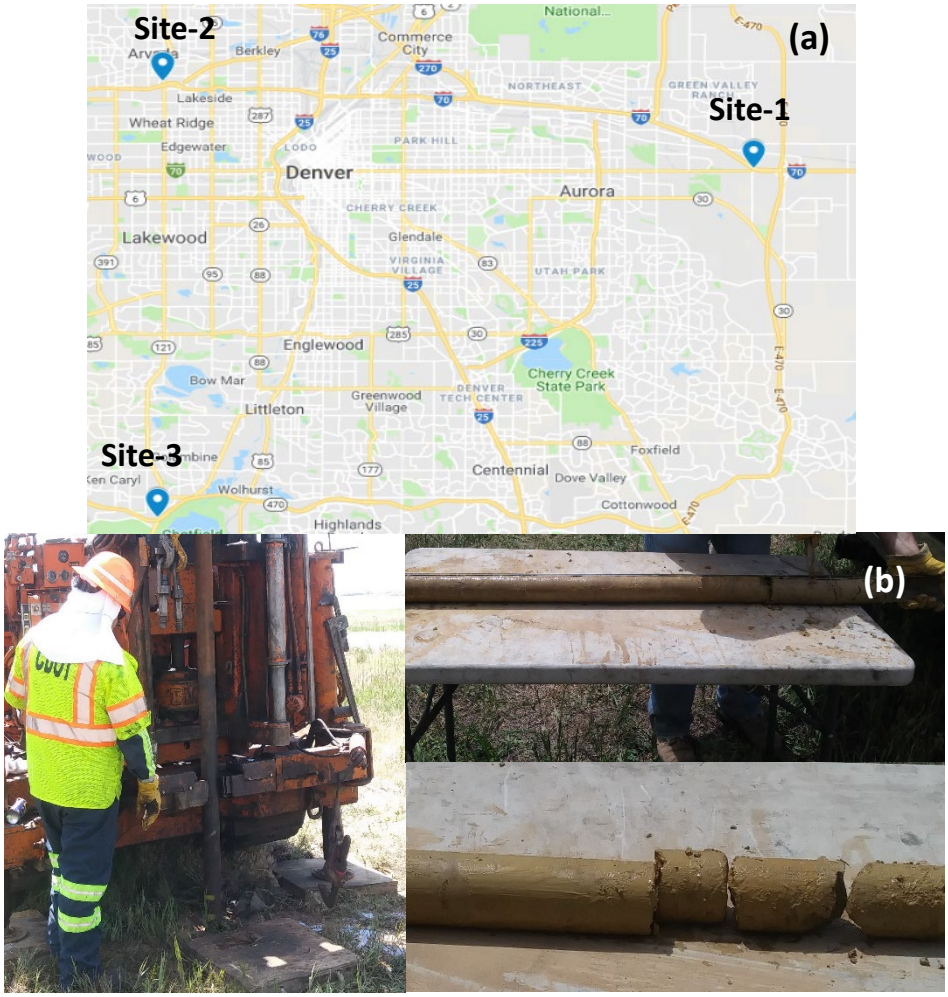

Figure 1. Sample drilling sites: (a) location on the map; (b) drilling pictures from site-1.

2.2 Vapor equilibrium

A critical step of this study is to prepare partially saturated samples with uniformly distributed degree of saturation throughout the sample. To achieve this, it was decided to control the saturation through vapor equilibrium technique (Pineda et al., 2013). Vapor phase equilibrium is achieved by placing the samples in a sealed desiccator together with saturated salt solution. The salt solution and the sample are not in contact at any point of time. Instead, the samples exchange water vapor with the ambient air in the desiccator till equilibrium was reached. The saturated salt solution serves as a regulator of the relative humidity in the desiccator which also provides a constant and uniform suction pressure to the sample. The total suction can be computed from relative humidity via the Kelvin's law (Coussy and Franz 1995).

$$\psi = \frac{RT\rho_w}{M_w}\ln(RH) \quad (1)$$

Here R=8.314 J/(K.mol) is the gas constant, $T = 293$K is the absolute room temperature; $M_w = 18$g/mol is the molecular mass of water; ρ_w is the density of pure water; ψ is the total suction and RH is the relative humidity in fraction. To ensure the salt solution is always saturated, extra undissolved salt is added to the solution to serve as a reservoir. As water vapor is constantly drawn into the solution, more salt will be dissolved to keep the solution saturated. A schematic of the desiccator and a picture of the laboratory setup is shown in Figure 2. Temperature of the laboratory is kept relatively constant $20^0C \pm 2^0C$ throughout the project.

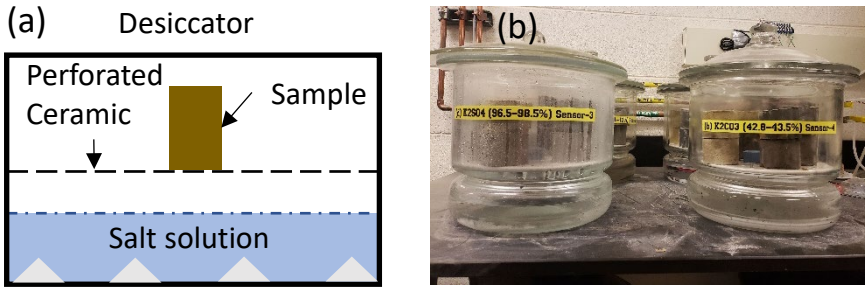

Figure 2. Vapor phase saturation method; (a) schematic; (b) picture of laboratory setup.

Four different salt solutions corresponding to different suction pressures are used to prepare samples with four different degree of saturations as listed in Table 3. The salts are selected to represent a broad range of suction pressure and at the same time to avoid the use of highly toxic substances. The desiccators are also used to generate the high suction points on the SWRC curve as explained in the next subsection.

Table 3. Salt solutions used and resulting total suction in Vapor phase saturation method.

Desiccator	Salt Solution	Avg. RH (%)	Avg. Suction (MPa)
a	$LiCl$	11.31	294.29
b	K_2CO_3	43.16	113.46
c	$NaCl$	75.47	38.00
d	K_2SO_4	97.59	3.29

2.3 Soil water retention curve (SWRC)

It is well known that he SWRC curve exhibits hysteresis over the complete cycle of wetting and drying. Which means that the SWRC curve has different branches for the wetting and drying paths, as shown schematically in Figure 3.

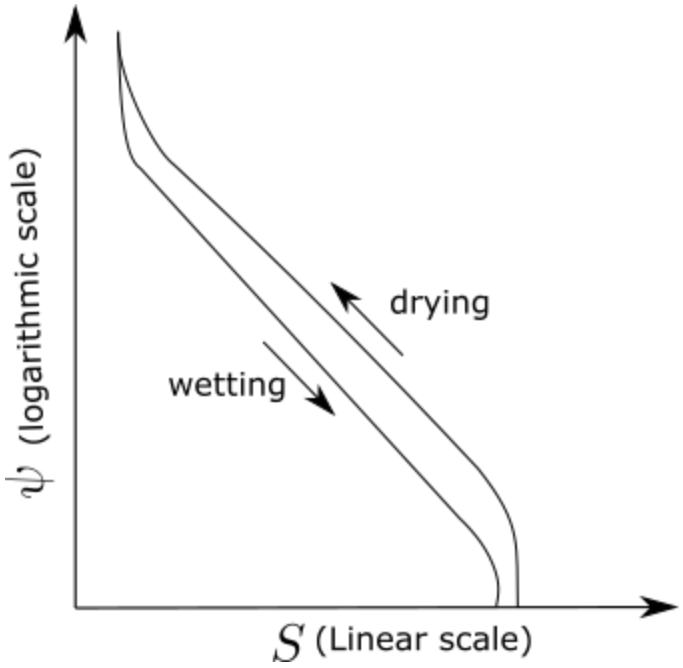

Figure 3. Schematic of typical SWRC curve with wetting and drying branches.

Considering the project focuses on wetting induced degradation, we measured the wetting branch of the soil water retention curves for all samples. Each curve is constructed using two test setups: vapor equilibrium for high suction range and Tempe cell for low suction range. Both experiments provide data points of suction pressure and corresponding water content, the water content is then converted to the degree of saturation by normalizing it with the saturated water content. Since clay-bearing rocks are susceptible to swelling, the meaning of saturated water content can be ambiguous. In this study, the saturated water content is defined as the water content at which the claystone sample is equilibrated with the oedometric condition with the top open to atmosphere allowing free swelling and bottom in contact with deaired deionized water. The same method is used for all the sites for consistency.

For each site, samples from shallow and deep depths are tested for four different suction pressures. For each suction pressure and depth, two disk-shaped samples with a mass of about 40g are tested, and the average value is used to generate the SWRC curve. The samples are first oven dried and

then placed in desiccators with different salt solutions to reproduce a wetting path. The desiccators are then carefully sealed with vacuum grease. The samples are taken out every five to six days to measure the mass change due to vapor exchange with the desiccator. The variation of mass with time, for representative samples from the three sites, is shown in Figure 4. Initially, dried samples quickly adsorb moisture in the air resulting in a rapid increase of sample mass with time. The rates of moisture adsorption and mass change then become slower over time until an equilibrium state is reached. Based on these observations, an incubation time of one month was considered adequate to prepare the specimens for the direct shear tests. The water content of the equilibrated samples together with the corresponding suction pressures of the desiccators is used to develop the SWRC data points at high suction range.

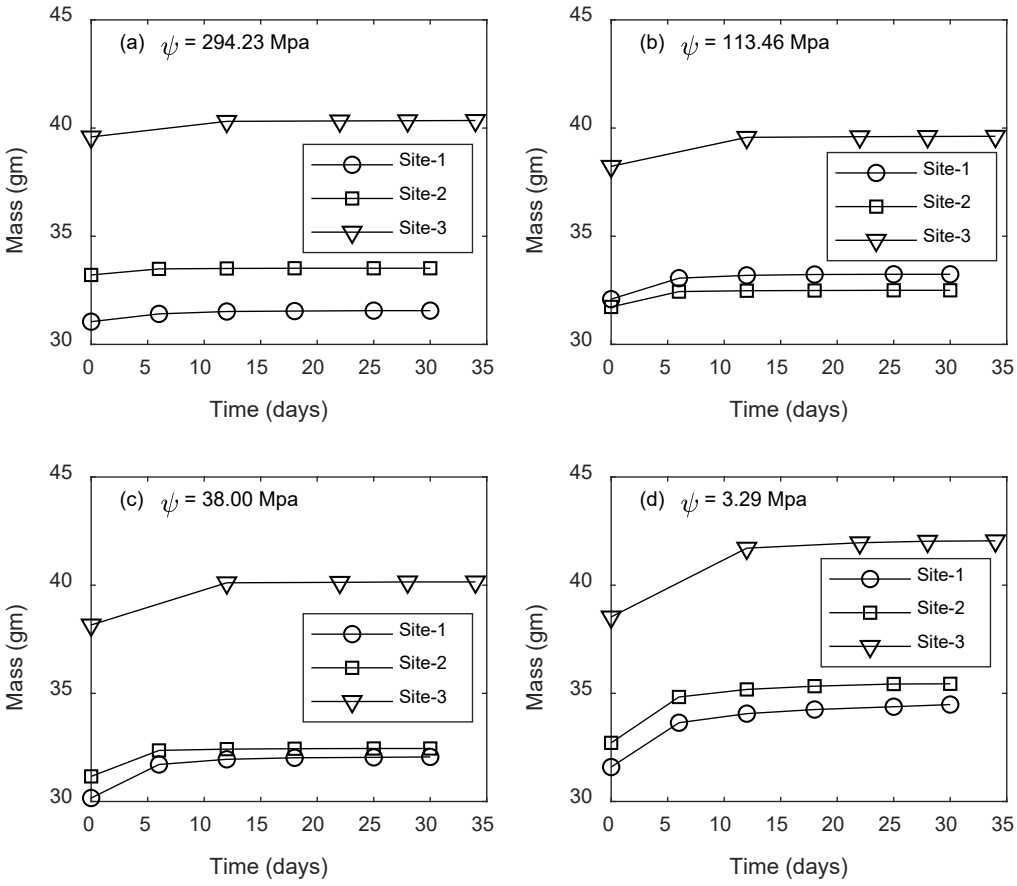

Figure 4. Variation of SWRC sample mass with time during vapor equilibrium.

One additional point in the low suction range (200 kPa) is generated by using a modified Tempe cell setup for wetting. The setup consists of a traditional Tempe cell with the outlet connected to a burette. The samples are prepared by pressing the Tempe cell ring over a larger Claystone core in

a manner similar to the core-cutter method. The sample is oven dried and the dry mass is determined (including the ring). Prior to the experiment, the high-air-entry (HAE) porous disk is saturated by boiling in water. At the start of the experiment, the HAE disk and the sample are placed in the Tempe cell, all tubes are filled with deaired water and the valve to the sample are closed. A suction pressure of 200 kPa is then applied through compressed air. The valve is then opened to allow for inflow of the water and thus the wetting of the sample. The change in the water level in the burette is recorded at regular intervals. Once the water level in the burette became steady, the sample is removed, and the water content is measured to produce the low suction point on the SWRC curve. The experimental setup is shown in Figure 5.

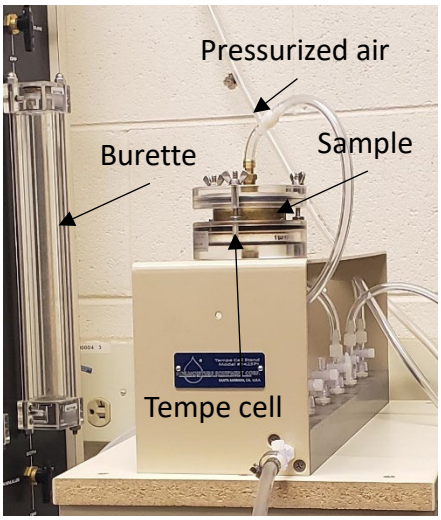

Figure 5. Tempe cell setup for low suction point on SWRC curve.

The experimental data points were fitted by the Van Genuchten equation (Van Genuchten 1980) to generate the final SWRC curves to be used in the numerical analysis, in the form of:

$$\frac{S - S_r}{1 - S_r} = \left(\frac{1}{1 + (\alpha\psi)^n}\right)^{1-\frac{1}{n}} \quad (2)$$

where S is the degree of saturation, S_r is the residual degree of saturation, ψ is the total suction, α is a parameter approximately equal to the inverse of the air entry suction and n is the parameter governing the steepness of the SWRC. For each site, two SWRC curves are generated, one corresponding to the deep and one corresponding to the shallow sample. The calibrated parameters for the Van Genuchten equation are listed in Table 4 and the fitted SWRC curves along with the experiments data points are shown Figure 6a. The generated SWRC curves are also compared with

the experimental data reported by Lu et al. (2014) in Figure 6b. It can be seen that the SWRC curves are in good agreement with the data obtained in the current study as well as in the literature.

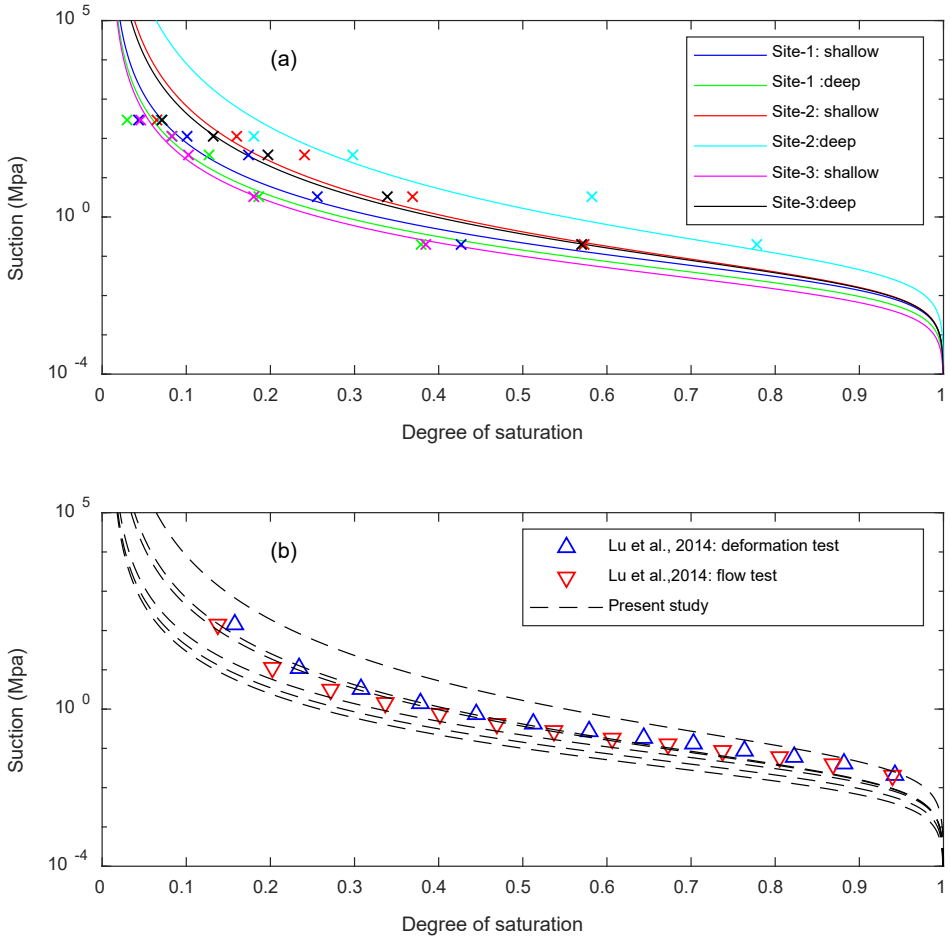

Figure 6. SWRC curves: (a) experimental data fitted with Van Genuchten equation; (b) comparison with Lu et al. (2014)

Table 4. Parameters of the fitted Van Genuchten equation for SWRC

Site	Sample	$\alpha(kPa)^{-1}$	S_r	n
1	Shallow	0.05	0.01	1.29
1	Deep	0.07	0.01	1.30
2	Shallow	0.05	0.01	1.23
2	Deep	0.02	0.01	1.20
3	Shallow	0.1	0.01	1.30
3	Deep	0.05	0.01	1.24

2.4 Direct shear test

The Direct shear specimens are prepared at four different suction pressures again using the vapor equilibrium technique. For each value of suction, at least three tests at different normal stress are conducted to produce the peak and residual strength envelope. The exact number of tests varies for different sites depending on the sample availability and variability. The specimens have a cylindrical geometry with an approximate height of 45 mm. The diameter of the specimens, after vapor equilibrium, varies between 60 to 64 mm. Part of this variation is caused by the natural variability of sample provided and part is due to swelling/shrinkage during the partial saturation process in the desiccator. All the specimens are tested immediately after their removal from the desiccator to minimize moisture perturbation. Because of this time constraint, the use of encapsulating material between the specimen and the regular direct shear box for rocks is not possible as the time required for the hardening of the encapsulating material would have resulted in significant moisture alternation. As a result, the testing procedure recommended by ASTM standard D5607-26 could not be used here. Instead, a cylindrical direct shear box with central split is designed and fabricated to secure the sample tightly and rapidly.

2.4.1 Shear box design

The direct shear box consists of a loading cap, a top ring and a bottom ring connected to a bottom plate as shown in Figure 7. Both the top and bottom rings consist of two semi cylinders that are connected through three nuts and bolts on each side. The separation between the semi-cylindrical sections is adjustable to accommodate samples of different sizes.

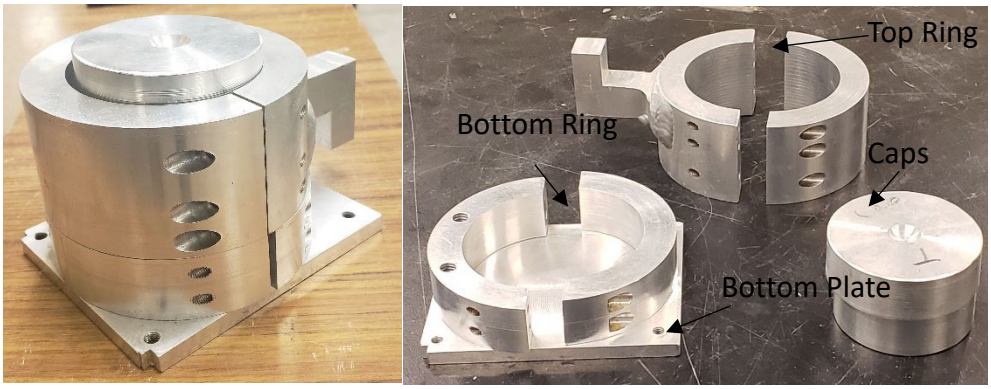

Figure 7. Direct shear box with individual parts.

2.4.2 Sample preparation

Direct shear samples of an approximate length of 45 mm are directly cut from the core samples. Samples are placed in the desiccators immediately after cutting and kept in there for one month in an undisturbed state prior to testing. The weight, height and diameter are recorded. The height and diameter are recorded at three different places and the average is used.

2.4.3 Procedure

First, the top and bottom rings are dissembled, and some oil is applied between them for lubrication. Then, the specimen is taken out of the desiccator and placed at the center of the bottom plate such that, it is in touch with the half part of the bottom ring. The other part of the bottom ring is then connected to the first part with nuts and bolts so that, the sample is well secured in the bottom ring (Figure 8a). Then, two thin rods of thickness 2.4 mm are placed on the sides of the bottom ring and, the top ring is assembled in a way that the gap between the two rings is uniform. Then, the nuts on the top ring are tightened to secure the sample in the top ring, and the rods are removed. After the assembly of the shear box, with the sample in it, the unit is placed on the direct shear machine and the base is rigidly connected to the base of the machine using four nuts (Figure 8b). From here on, the testing procedure is similar to the traditional direct shear test. The normal load is applied and the vertical and horizontal LVDT are connected. The sample is then sheared at a rate of 1 mm/min till the residual state is reached or ten minutes have passed. The peak and residual horizontal forces are measured from the force displacement curve to plot the peak and residual failure envelopes.

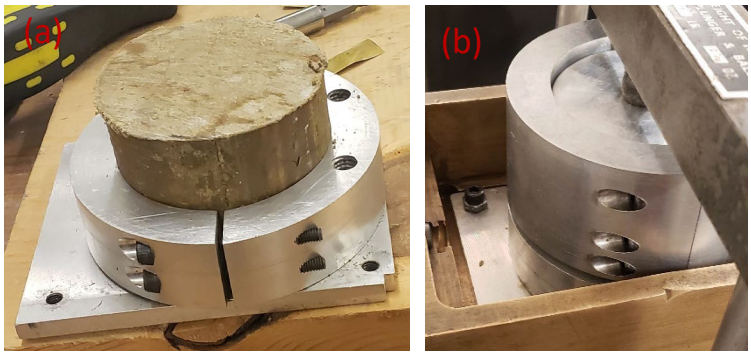

Figure 8. Sample placement in the direct shear box; (a) bottom half assembled; (b) entire box assembled and connected to the searing machine.

2.4.4 Results

A typical set of load-displacement curve from the direct shear test is plotted in

Figure **9**. These curves correspond to site-1 specimens subjected to the same normal load but prepared at different levels of suctions (degree of saturation). The peak and residual states are marked on the figure for one of the curves. As seen from the figure, the specimens prepared at higher suction (lower degree of saturation) have higher strength with brittle response. The load-displacement curve becomes more ductile and the strength reduces as the suction decreases. Photos of high-suction and low-suction specimens after shearing are shown in Figure 10. It can be seen that the failure plane of the specimen prepared at low suction is more uniform (Figure 10a), while that of the specimen prepared at high suction is more irregular (Figure 10b). These observations from

Figure **9** and Figure 10 can be related to the role of microcracks in the rock specimen. At low suction, the intrinsic shear strength of the bulk material is low and thus governs the failure response of the specimen, resulting in ductile response and a uniform failure plane. In contrast, at higher suction, the intrinsic shear strength of the rock matrix is higher, and the failure is governed by the presence of microcracks. As the sample is sheared, microcracks are mobilized and extended until suddenly coalesced, forming an irregular failure plane. As a result, a sudden drop of shear stress in the load-displacement curve is observed. In summary, at low suction (high degree of saturation) the intact material strength governs the overall specimen strength, while at higher suction (lower degree of saturation) the heterogeneity of the specimen (i.e. microcracks) governs its strength.

The peak and residual failure envelopes of the claystone from the three sites at different suction pressures, along with the experimental data points, are shown in Figure 11 to Figure 13. As expected, it is observed that both the peak and residual strength decrease with decrease in suction pressure or increasing degree of saturation. The most likely source of scatters in the data is the presence of small cracks in undisturbed samples, and the larger scatter in the data from site-1 and site-3 indicates that the effect of microcracks is more profound for the samples with higher strength. This is consistent with the previous observation that the apparent strength of samples with higher intrinsic strength is likely governed by internal heterogeneities and microcracks. Another observation is that the residual cohesion is zero for all the sites irrespective of the suction pressure. This is reasonable considering that at the residual stage, all the bonds along the failure

plane have been already broken, and the remaining shear resistance is solely resulted from the frictional forces acting on the failure plane. The peak and residual Mohr-Coulomb parameters obtained from Figure 11 to Figure 13 by fitting the equation of Mohr-Coulomb failure line to the experimental data. The Mohr-Coulomb failure line for peak total stress is given by equation (3) as shown below.

$$\tau = c_p + \sigma_n \tan \phi_{\mathrm{p}} \tag{3}$$

where, τ is the shear stress on the failure plane at peak of axial stress-strain curve, σ_n is the total normal stress on the failure plane at peak of axial stress-strain curve, c_p is the peak apparent cohesion and ϕ_p is the peak apparent friction angle. The Mohr-Coulomb failure line for residual total stress is given by equation (4).

$$\tau = c_r + \sigma_n \tan \phi_r \tag{4}$$

where, τ is the shear stress on the failure plane at residual stage of axial stress-strain curve, σ_n is the total normal stress on the failure plane at residual stage of axial stress-strain curve, c_r is the residual apparent cohesion and ϕ_r is the residual apparent friction angle. The peak and residual Mohr-Coulomb parameters thus obtained are summarized in Table 5.

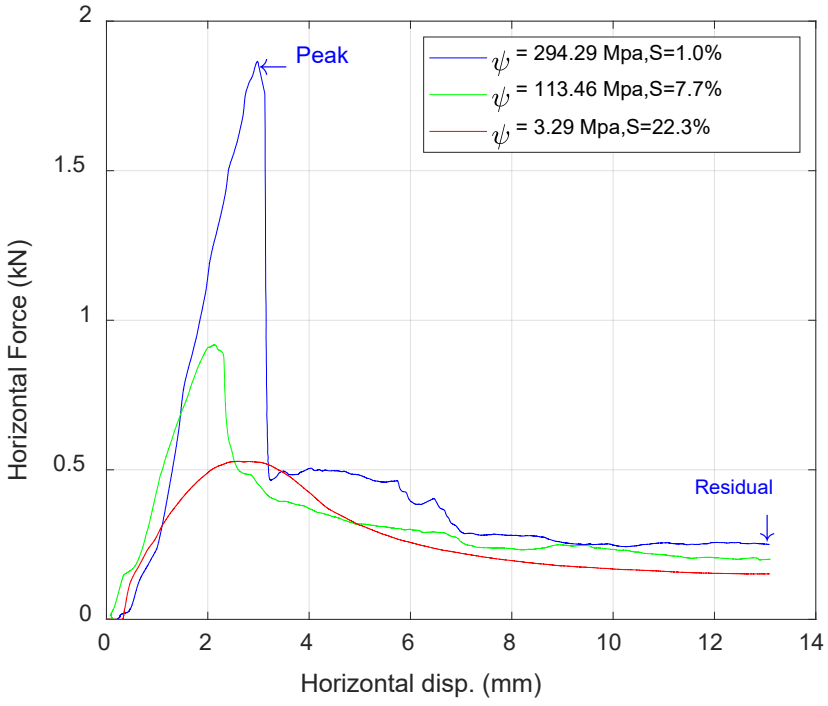

Figure 9: Typical direct shear load-displacement curves.

Figure 10: Specimen before and after shearing: (a) low suction; (b) high suction

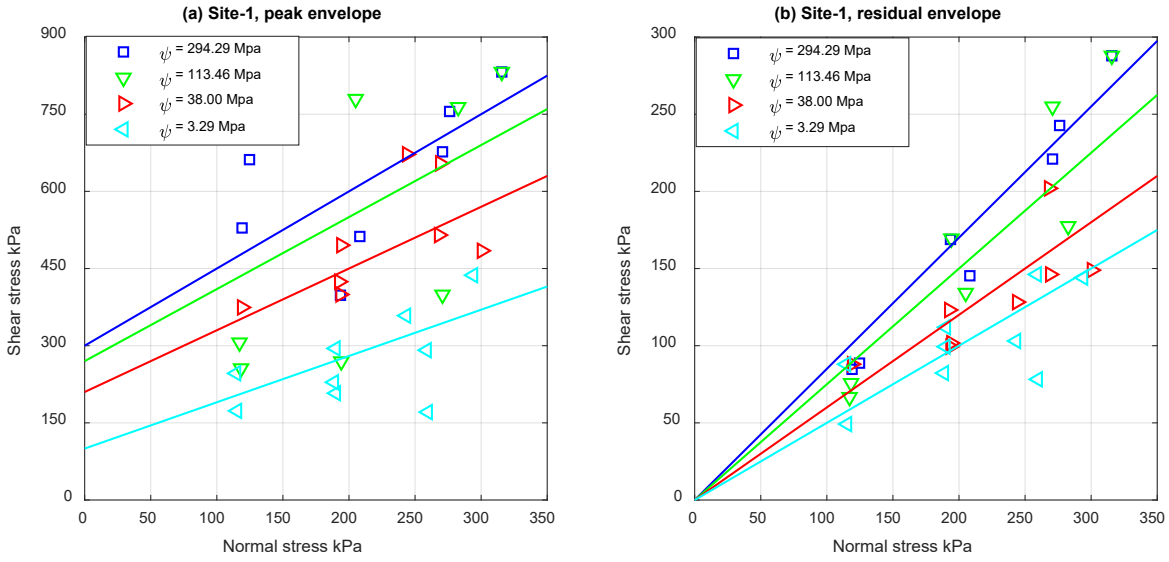

Figure 11. Mohr-Coulomb strength envelopes at different suctions for site-1; (a) peak strength; (b) residual strength.

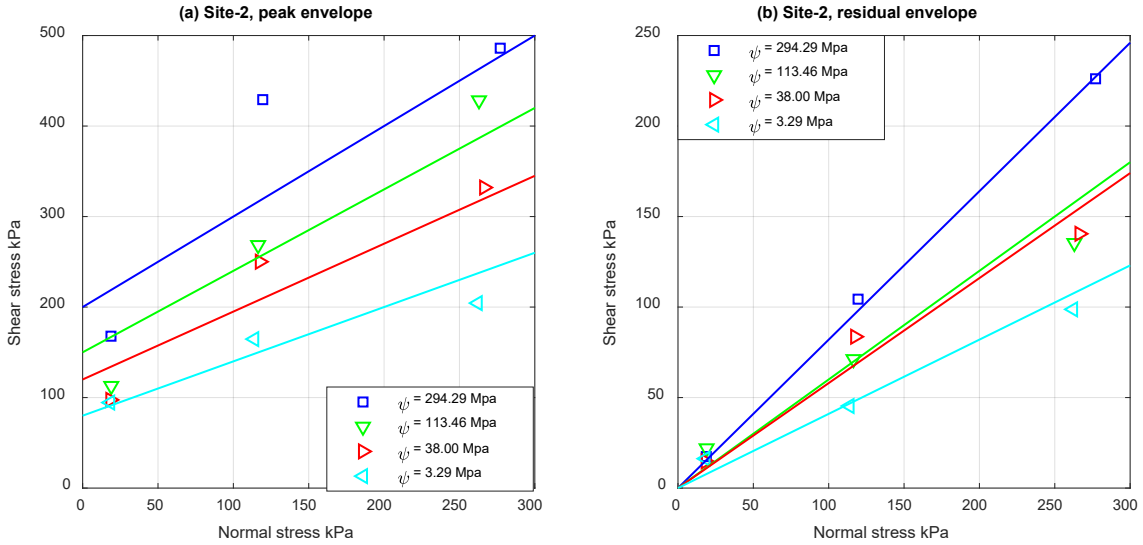

Figure 12. Mohr-Coulomb strength envelopes at different suctions for site-2; (a) peak strength; (b) residual strength.

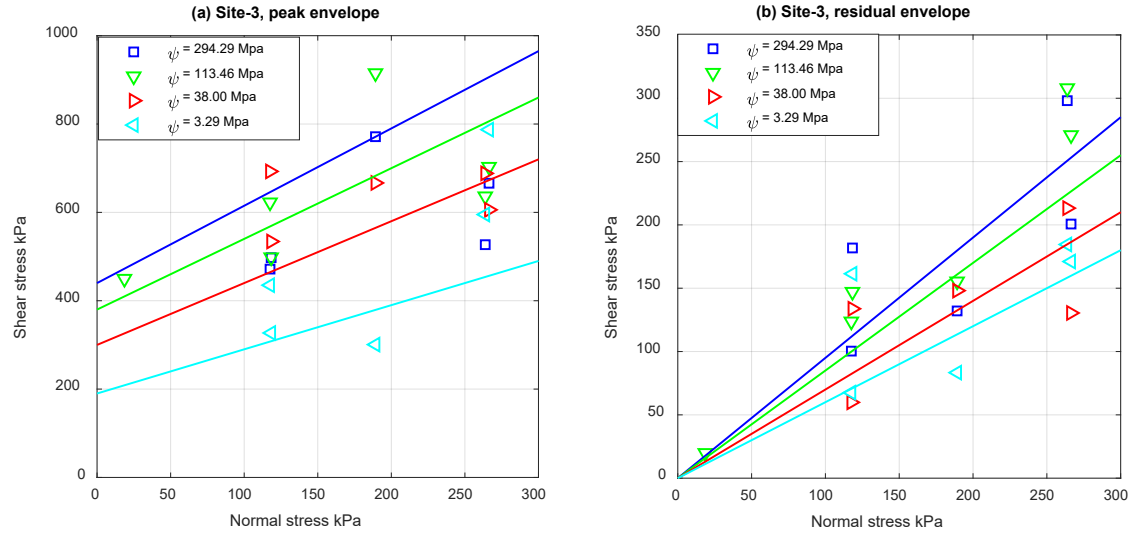

Figure 13. Mohr-Coulomb strength envelopes at different suctions for site-3; (a) peak strength; (b) residual strength.

Table 5. Peak and residual Mohr-Coulomb strength parameters

Site	Suction ψ (Mpa)	Peak friction angle ϕ_p	Peak cohesion $c_p(kPa)$	Residual friction angle ϕ_r	Residual cohesion $c_r(kPa)$
1	294.29	56.31	300	40.36	0
	113.46	54.46	270	36.87	0
	38.00	50.19	210	30.96	0
	3.29	41.99	100	26.57	0
2	294.29	45.00	200	39.35	0
	113.46	41.99	150	30.96	0
	38.00	36.87	120	30.11	0
	3.29	30.96	80	22.29	0
3	294.29	60.26	440	43.53	0
	113.46	57.99	380	40.36	0
	38.00	54.46	300	34.99	0
	3.29	45.00	190	30.96	0

The variation of ϕ_p , ϕ_r and c_p with respect to suction is plotted in Figures 14 and 15, respectively. The tangent of the peak and the residual friction angles are fitted using a log-linear relationship with respect to suction pressure:

$$tan(\phi_p) = a_p \log\left(\frac{\psi}{\psi_{ref}}\right) \quad (5)$$

$$\tan(\phi_r) = a_r \log\left(\frac{\psi}{\psi_{ref}}\right) \quad (6)$$

Here, ψ is the suction pressure in kPa; $\psi_{ref} = 1kPa$ is reference suction; ϕ_p and ϕ_r are the suction dependent peak and residual friction angles respectively; a_p and a_r are the corresponding fitting parameters. The fitted curves are plotted in Figure 14.

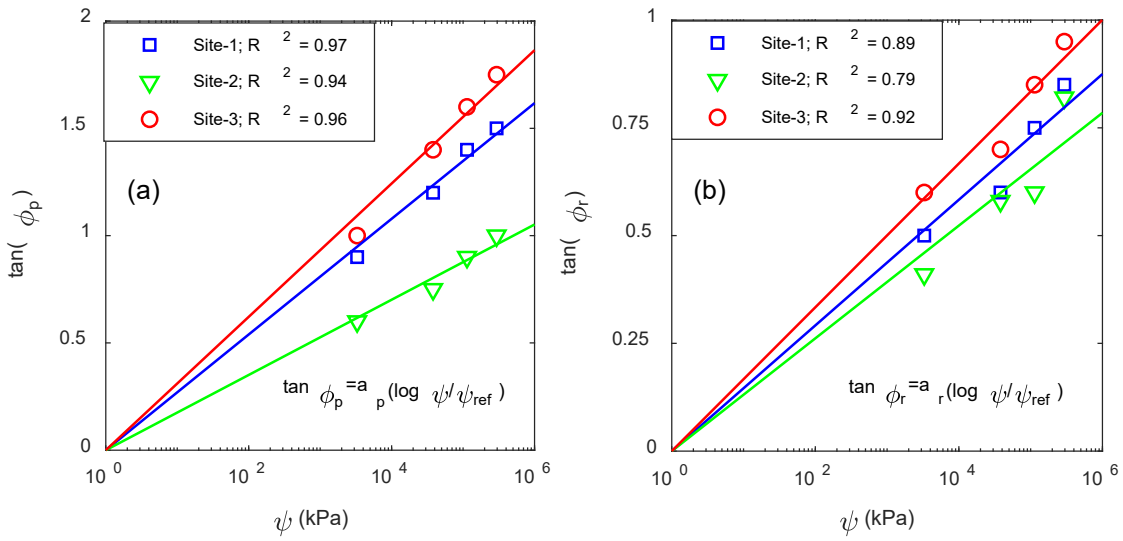

Figure 14. Variation of friction angle with suction pressure; (a) peak friction angle; (b) residual friction angle.

The cohesion-suction data for the peak envelope is plotted in Figure 15 with open symbols. Observing the nonlinear nature of these trend in the semilogarithmic plot, additional direct shear tests were conducted on fully saturated samples with nominal normal stress to determine their intersections with the y-axis. They are also shown in Figure 15 marked by solid symbols. Based on this data, the peak cohesion is fitted with log-quadratic curve by:

$$c_p = c_{p1} + c_{p2}\left(log\frac{\psi}{\psi_{ref}}\right)^2 \tag{7}$$

Here, c_p is the suction dependent peak cohesion in kPa; c_{p1} and c_{p2} are the two fitting parameters in kPa; ψ and ψ_{ref} have the same definition as before. It is worth noting that the fitted curves are only applicable for suction higher than the reference value, the strength parameters are taken to be constant below the reference suction. The values of fitting parameters for all three sites are listed in Table 6.

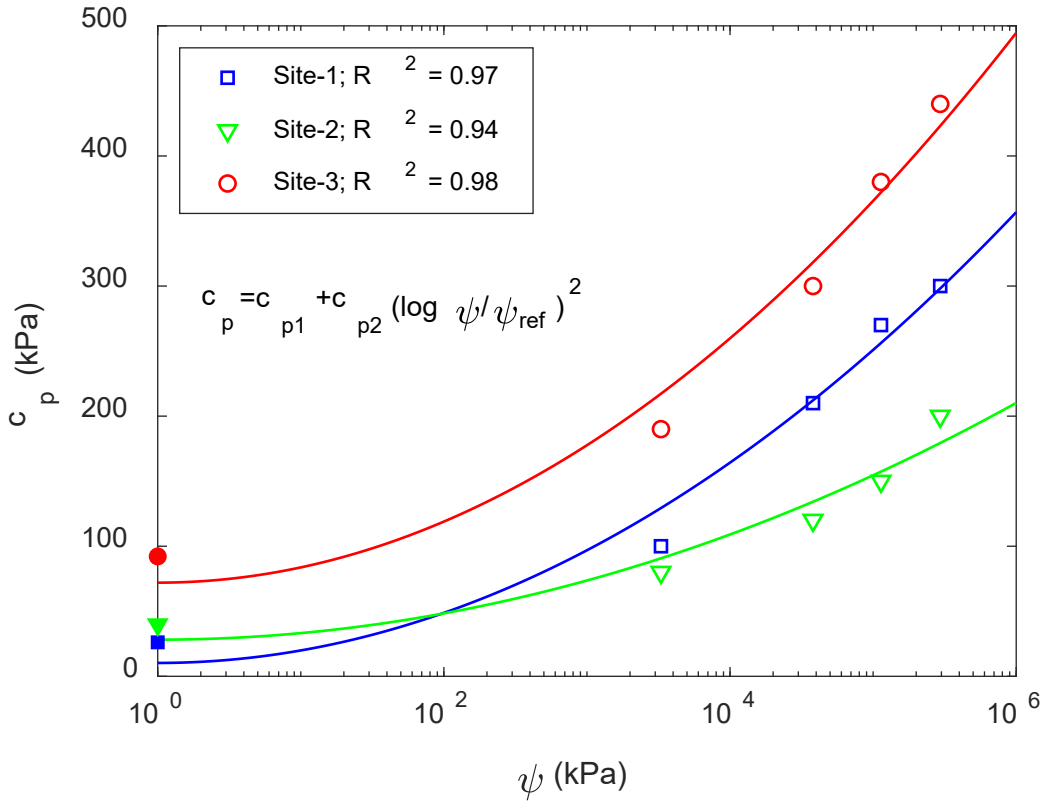

Figure 15. Variation of peak cohesion with suction pressure.

Table 6. Parameters for the fitted relation between strength and suction pressure.

Site	a_p	a_r	$c_{p1}(kPa)$	$c_{p2}(kPa)$
1	0.2696	0.1458	10.28	9.625
2	0.1753	0.1308	28.18	5.055
3	0.3107	0.1458	72.00	11.740

2.5 Interface direct shear test

The direct shear tests for the interface strength were planned, but the sample preparation for this test was found to be impractical and the test had to be abandoned. The initial idea was to cut a 22-23 mm high sample from the core and put it in a mold. The mold was designed such that water could be inundated on the top of the sample without any leakage from the sides. It was planned to cast concrete on the top of the sample after water inundation to prepare the interface direct shear sample. The time lapse between the water inundation and concrete placement would have served as wetting time. It was expected that a thin zone of degraded Claystone will form at the rock-

concrete interface, governing the interface shear strength. Preliminary experiment setup consisted of a temporary mold made from plastic bottles (Figure 16a) with wax placed between the sample and the mold. This method was successful in preventing side leakage during water impoundment. However, it was unexpected that a much larger degraded zone has formed in the preliminary test even at wetting time as small as thirty minutes (Figure 16b,c,d). From this we concluded that the degraded zone at the pile-bedrock interface extends to great distances, much larger than the applicable range of the interface direct shear tests. Therefore, the experiments were abandoned. In the numerical model presented the next section, the rock-concrete interface was modeled as frictional boundary with a constant friction coefficient. The degradation of side friction resistance is indirectly captured by the formation of a fully softened rock mass zone along the caisson periphery, in the wetting stage of the simulation. This is consistent with the observation of a large softening zone in the interface direct shear test attempts, and the observations of Claybourn (2007) during the post failure analysis of a caisson failure in Colorado Front Range.

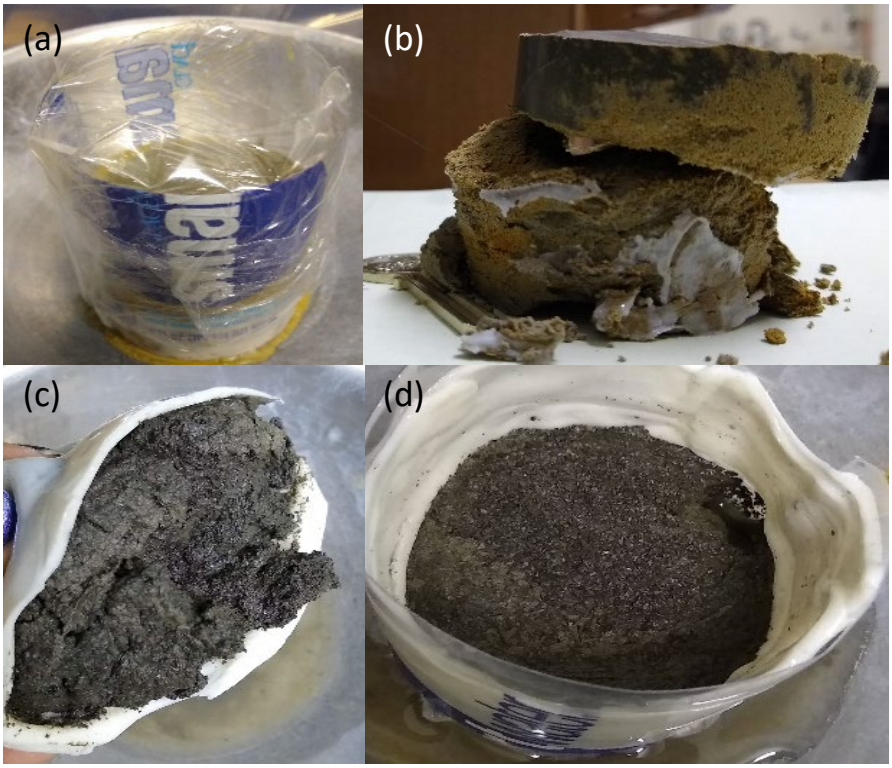

Figure 16. Preliminary Interface direct shear test sample preparation; (a) temporary plastic mold; (b) the concrete and the claystone parts immediately detached following the proposed procedure; (c,d) highly degraded samples after thirty minute water inundation.

2.6 Hydraulic conductivity

The saturated hydraulic conductivity values of the specimen are obtained using the Flex-wall permeameter (Figure 17) in accordance with the ASTM: D5084-16a, method-C. Samples with an aspect ratio between 1.3 to 1.5 are tested. The sample length was restricted by the presence of cracks in the core since we tried to void any visible cracks in the sample. The test consists of three phases: soaking in first phase; back-pressure saturation in second phase and hydraulic conductivity measurements are made in the third phase. For all the tests: 5 psi cell pressure and vacuum top pressure is applied during soaking stage, 10 psi cell pressure and 5 psi back pressure is applied during back pressure saturation, and the applied initial hydraulic gradient, during the hydraulic conductivity measurement, varied depending on the sample. The measured hydraulic conductivities along with the testing conditions are listed in Table 7.

Table 7. Saturated Hydraulic conductivity.

Site	Cell pressure (psi)	Backpressure (psi)	Initial head difference (in)	Hydraulic conductivity (ft/sec)
1	10	5	77.66	7.12×10^{-10}
2	10	5	8.724	8.01×10^{-08}
3	10	5	8.724	1.88×10^{-07}

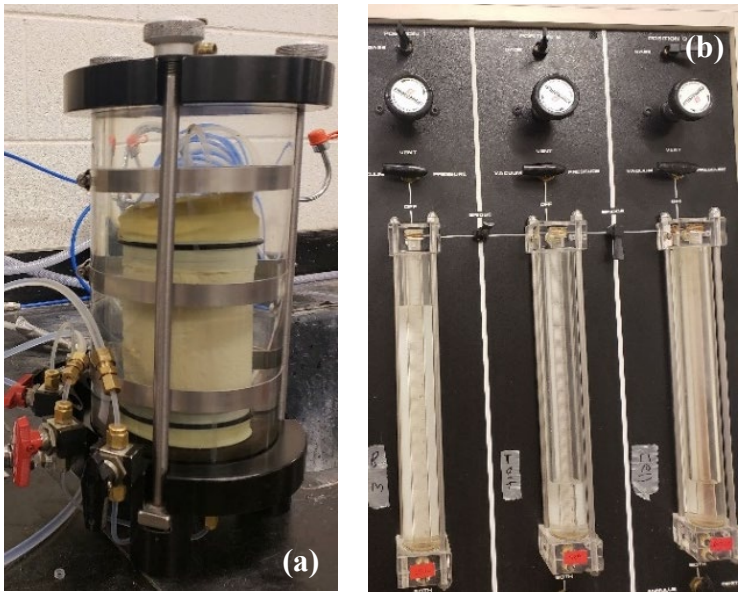

Figure 17. Hydraulic conductivity measurement setup a) Flex wall permeameter; b) pressure-volume panel

3. FINITE ELEMENT MODEL

3.1 Introduction

A hydromechanically coupled Finite Element Analysis (FEA) is conducted to predict the degradation of axial load capacity at the three sites based on the experimental data. The FEA is performed using the general-purpose Finite Element Package ABAQUS. ABAQUS provides a user-friendly interface for model generation and postprocessing interface for analyzing the simulation results. Both explicit and implicit time integration options are available in ABAQUS solvers. Considering the relatively moderate size of the simulations, the unconditionally stable implicit time integration scheme is adopted in this study. A coupled pore fluid diffusion and stress analysis (i.e. "soil" type analysis) is used to model partially and fully saturated fluid flow through deformable porous media. The unsaturated flow through the porous media is governed by the generalized Darcy's law given by equation (8)

$$q_i = -k_r K \frac{\partial\left(\frac{p}{\rho_w g} + z\right)}{\partial x_i} \tag{8}$$

where i=1,2,3 indicates free index; q_i is the flux of pore water flow; K is the hydraulic conductivity of water through fully saturated porous media; p is the pore water pressure, ρ_w is the density of water, g is the gravitational acceleration; $z = x_3$ is the depth; and k_r is the relative permeability that varies with degree of saturation. Abaqus permits user-defined relationships between the relative permeability and the degree of saturation, allowing the pore water flow to depend on the degree of saturation for partially saturated flow. The constitutive model for porous media is formulated based on the effective stress with small strain assumption. The Bishop's effective stress definition is adopted to define the effective stress for unsaturated conditions as discussed later in this section. The constitutive equations of the porous media can be selected from the build-in material library or customized via the user-subroutine options offered by ABAQUS. The material library includes a large range of plasticity models such as Ducker-Prager, von Mises, Mohr-Coulomb, and Cam Clay. In this study, the Mohr-Coulomb plasticity model with linear elasticity and perfect plasticity from the build-in material library is used. The shear strength is governed by the Mohr-Coulomb failure criterion based on Bishop's effective stress:

$$\tau = \sigma_n' \times \tan(\varphi') + c' \tag{9}$$

where τ is the shear stress on the failure plane at yielding, σ'_n is the effective normal stress on the failure plane, c' is the effective cohesion and ϕ' is the effective friction angle. The effective cohesion and effective friction angle are calibrated using the experimental results in terms of the total peak cohesion and friction angle. The process of calculating effective strength parameters based on the total strength parameters obtained in section 2.4 is explained in section 4. With the constitutive laws for the porous media and the pore fluid specified, the program iteratively solves the diffusion equation (or mass balance of water) and equilibrium condition using fully implicit Newton-Raphson algorithm. In this project we will take advantage of the user-defined field subroutine (USDFLD) feature to update the strength parameters of claystone with respect to changing hydraulic field variables (saturation and pore pressure in this case) during each iteration. In the following, a simple axisymmetric finite element model containing the bedrock and pile is built in ABAQUS first (section 3.2). All the input parameters such as soil-water characteristic curve, strength saturation relation and basic index properties are determined from the experimental results presented in section 2, with some elastic parameters extracted from existing literature (section 3.3). In order to reproduce realistic construction sequence, the full process of wet construction method including drilling, wetting and pile installation are simulated prior to in-situ axial load testing (section 3.4).

3.2 Model geometry and mesh type

An axisymmetric model of a single pile socketed in claystone is built. The geometry of the model is decided based on the field test data from Abu-hejleh et al. (2005) and is sketched in Figure 18. The soil above the claystone formation (approximately 29ft deep) is not included in the model but idealized as an overburden pressure. Considering the moist unit weight of soil to be 105 pcf, the total overburden pressure is calculated as 3045 psf. Similarly, 19 ft of the pile below the ground surface is replaced by an equivalent pressure of 2850 psf applied on top of the simulated pile segment. In all the baseline simulations, the depth of the water table is taken as 69 ft below the ground (25 ft below the pile tip). This location of water table is estimated using the data from a station situated in Douglas County which is closest to site-3. This station, maintained by United States Geological survey Colorado Water Science Centre (USGS.gov), has been recording the groundwater level for Denver Basin aquifer in Douglas county since 2011. Therefore, the data from 2011 to 2019 is considered and the average value is taken as the depth of water table in the simulation. The model consists a total of 916 elements with 866 elements in claystone and 50

elements in pile. CAX8P (eight-node axisymmetric quadrilateral, biquadratic displacement, bilinear pore pressure) element has been used in the simulation as it has degree of freedoms reserved for solid displacements and pore water pressure, permitting coupled hydromechanical analysis. The element size for the pile and the claystone meshes has been decided using the mesh recommendations provided in Sheng et al.(2005) and Bäker et al. (2018) . One of these recommendations suggests that the optimal size of claystone elements below the pile should be about one-half to one pile element in order to obtain convergent solution without introducing too much mesh error. Figure 18a and b show the schematics of the model geometry and finite element mesh of the model.

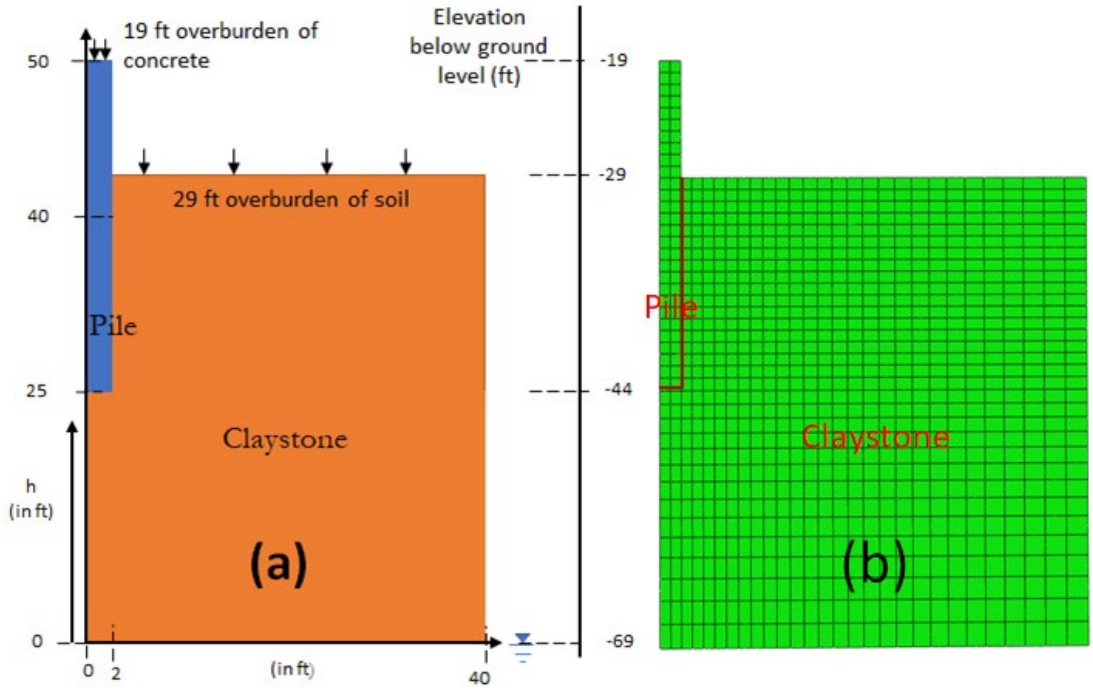

Figure 18. Model geometry (a) schematic and (b) finite element mesh

3.3 Input parameters

The input parameters for claystone are determined by the experiments described in Section 2. Due to the lack of stress-strain measurements, the representative elastic properties of the Denver Blue formation are taken from Abu-Hejleh et al. 2005 determined by in-situ testing. Claystone is modelled as a linear elastic perfect plastic material obeying Mohr-coulomb failure criterion in Bishop's effective stress space. The dilation angle is set to zero since the observed dilatancy in the direct shear test was small and varies from specimen to specimen (ranging between -2% to +10%).

The strength parameters such as effective cohesion and friction angle for claystone are assigned through a user-defined field subroutine (USDFLD) which will be detailed in section 4. The concrete pile is modelled as a linear elastic material with the Young's modulus and the Poisson's ratio taken from (Seo et al., 2008). The basic input parameters (except for strength parameters) for claystone and concrete are summarized in Table 8. The interface between claystone and pile is modeled as hard contact using penalty method. Nonlinear contact stiffness is assigned to avoid excessive overclosure at the interface. The friction coefficient of the pile-claystone interface is taken as 0.6.

Table 8. Input parameters

Parameters	Claystone			Concrete
	Site-1	Site-2	Site-3	
Saturated unit weight or density (pcf)	159.94	152.55	145.61	150
Young's modulus (psf)	7E+ 07	7E+ 07	7E+ 07	5.64E+08
Poisson's ratio	0.2	0.2	0.2	0.15
Saturated hydraulic conductivity (ft/sec)	7.13E-10	8.01E-08	1.88E-07	-

3.4 Steps used in the finite element simulation

The actual construction process of drilled caissons is simulated via five consecutive steps: geostatic balance, wetting, pile installation, friction activation at the interface, and axial loading test (Figure 19). Each step is detailed in the following subsections.

3.4.1 Geostatic balance

The geostatic balance is the very first step of simulating the in-situ stress condition in geotechnical problems. In this step, gravity is applied to the claystone with the pile deactivated. Ideally, the assigned internal stresses should exactly equilibrate the external loads so that zero deformation is produced after this step. However, in complex problems, it may be difficult to specify the exact equilibrating initial stresses compatible with the external loads. It is therefore desirable to get these stresses as close as possible such that the resultant strain field is below an allowable strain threshold after this step. Since ABAQUS performs the effective stress analysis, all the input parameters as

Schematic of the step	Step description	Total step time (sec)	Total time (sec)
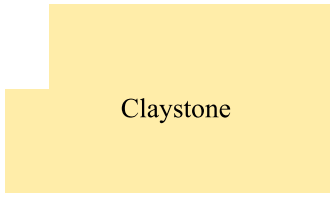	Step 1: Creating geostatic balance with a bore drilled in the claystone.	1	1
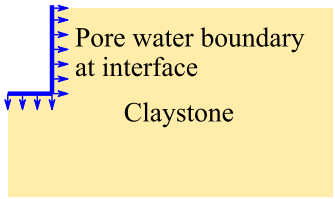	Step 2: Drilled fluid infiltration by applying a hydrostatic pore pressure boundary condition on the interface for 't' hours.	7200 (for 2-hour wetting)	7201
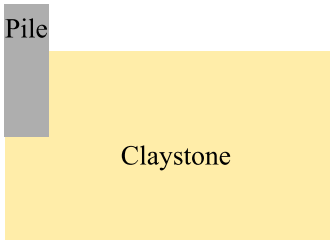	Step 3: Pile activation to simulate the placement of concrete in the borehole.	1800	9001
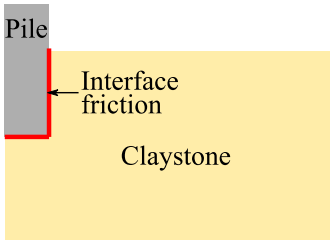	Step 4: Friction activation along the interface to simulater concrete hardening and bond development at the concrete-claystone interface.	7200	16201
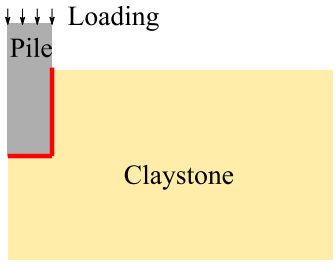	Step 5: Loading step at last to obtain the axial load-displacement curve of the pile.	7200	23401
*Here 't' in step 2 represents the different wetting time values which means the time between the drilling phase and the placement of concrete.			

Figure 19: Schematics of the steps used in the simulation

well as the initial stress field should be the effective values. To get the effective stress profile for the assigned SWRC and water table, a node path is created close to the right face of the model (Figure 20). The vertical effective stress (S22) and the degree of saturation data are exported along this path and collected in Table 9. In the table, the total stress is calculated by the Bishop's (1960) effective stress definition:

$$\sigma'_{ij} = \sigma_{ij} + \chi\psi\delta_{ij} \tag{10}$$

where σ'_{ij} is effective stress; σ_{ij} is total stress δ_{ij} is the Kronecker delta with $i,j = 1,2,3$; χ is Bishop's stress coefficient; ψ is the matric suction calculated by

$$\psi = -\gamma_w h \tag{11}$$

where h is the distance between the point of interest and the water table and γ_w is the unit weight of water. Refer to Figure 18a for the depth of the water table and the definition of h. Bishop's stress coefficient varies from zero for dry soil to unity for fully saturated soil. By default, ABAQUS takes χ as the degree of saturation S. Thus equation (10) becomes

$$\sigma'_{ij} = \sigma_{ij} + S\psi\delta_{ij} \tag{12}$$

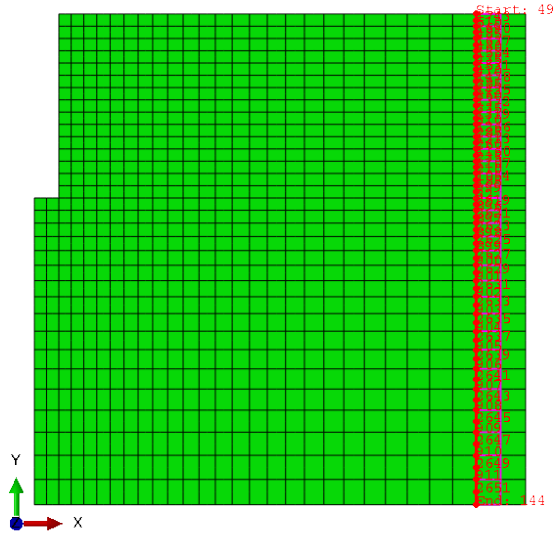

Figure 20. Path for extracting effective vertical stress (S22) and degree of saturation

Table 9. Extracted values along the path

Distance from base of the model, h (feet)	Effective Vertical Stress (psf)	Degree of saturation	Pore Pressure (psf)	Total Vertical Stress (psf)
40.00	-4650.38	0.6431	-2496	-3045.01
37.00	-5033.11	0.6530	-2308.8	-3525.38
34.00	-5419.97	0.6662	-2121.6	-4006.54
31.00	-5802.79	0.6793	-1934.4	-4488.59
28.00	-6181.55	0.6925	-1747.2	-4971.52
25.00	**-6560.22**	**0.7082**	**-1560**	**-5455.37**
22.15	-6919.39	0.7261	-1382.42	-5915.5
19.13	-7294.35	0.7452	-1194.2	-6404.41
16.32	-7644.37	0.7680	-1018.52	-6862.09
12.92	-8060	0.7977	-806.402	-7416.69
8.81	-8555.3	0.8456	-550.281	-8089.97
4.74	-9032.3	0.9089	-295.845	-8763.38
1.99	-9341.56	0.9614	-124.302	-9222.05
0.99	-9448.76	0.980	-9387.81	-62.1508
0	-9555.92	1	-9555.92	0

The initial stress field is assigned as a linear distribution with respect to the depth with the effective stress at the top and bottom nodes coincide with the ones obtained in Table 9. Since the pile is deactivated in this step, the side of the borehole is constrained by a slider boundary to prevent collapse. The potential heaving of the bottom of the hole is prevented by an overburden pressure equal to the total vertical stress at the level of pile tip (i.e., 25 feet from the base of the model; see Figure 18a) which is equal to 5455 psf (highlighted in Table 9). Figure 21a and Figure 21b shows the bottom heaving without and with the application of equivalent overburden pressure, respectively. The deformation in Figure 21 is exaggerated by a scaling factor of 10^4.

To determine whether the geostatic balance analysis is successful, the recommendations provided in ABAQUS (2016) documentation are followed:

- Ensuring that S22 (vertical stress component in axisymmetric model) is closer to the predefined geostatic field and contours in the visualization module for S22 are parallel.

- Ensuring that U2 (vertical displacement component in axisymmetric model) is very small and its contours are also parallel. Figure 21b shows that the U2 contours after the geostatic balance step is quite small (at the order of 10^{-5}) and Figure 22 shows that the S22 contours are parallel and close to what was define a priori. Thus, both conditions are satisfied, and the geostatic balance is successfully achieved.

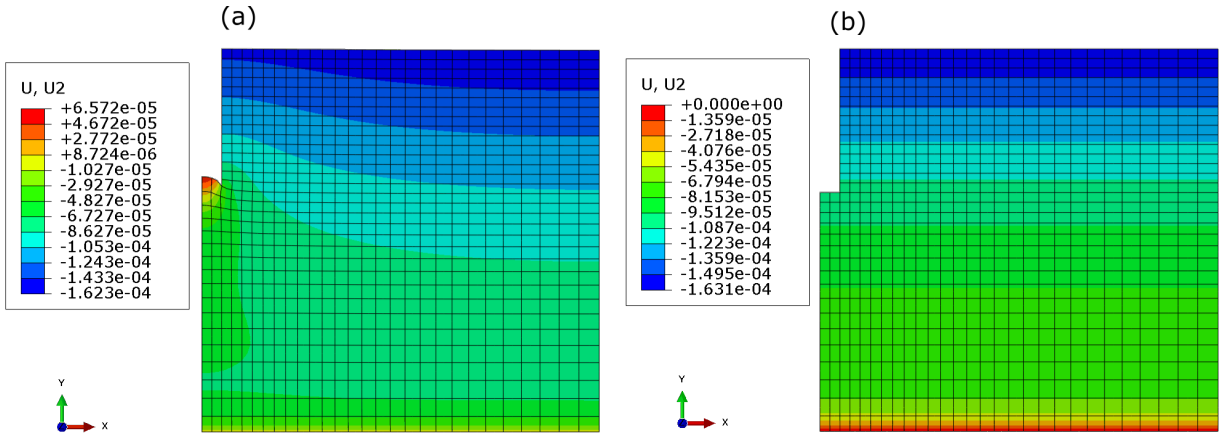

Figure 21. Vertical displacement contour (a) before and (b) after the application of equivalent overburden pressure at the bottom of the borehole

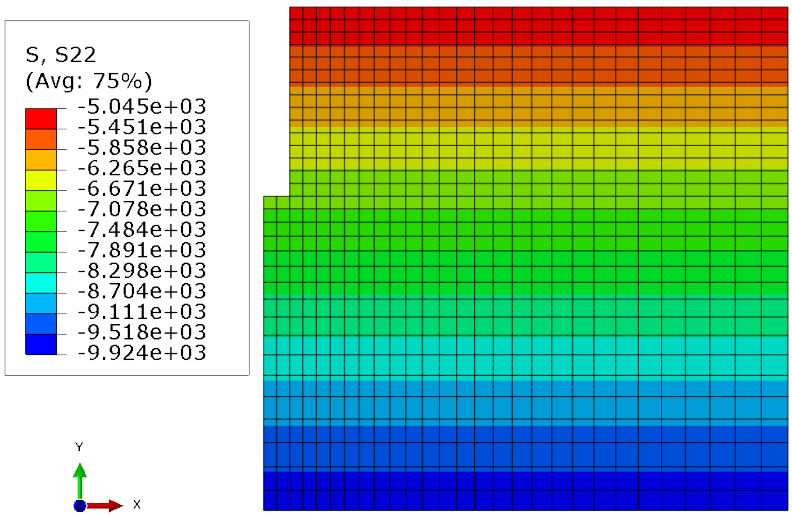

Figure 22. Vertical stress contours (S22) after geostatic step

3.4.2 Wetting phase

A wetting phase has been introduced to simulate the infiltration of drilling fluid in the claystone prior to concrete placement. In this analysis, four different wetting times (2 hours, 4 hours, 8 hours and 16 hours) have been tested, aiming to observe the level of decrease of the ultimate load capacity with increasing wetting time. Wetting was simulated by imposing a hydrostatic pore pressure boundary at the bottom and lateral surface of the borehole. Figure 23 shows the schematic diagram of the wetting step along with the pore pressure field applied at the interface. The corresponding pore water pressure profile along the boundary is summarized in Table 10.

The saturation contours for different wetting time for site 1, site 2 and site 3 are shown in Figure 24, Figure 25 and Figure 26, respectively. The red color in the figures represents the fully saturated regions. It is observed that for the same wetting time, site 3 has the largest wetting region while site 1 has the smallest infiltration depth. This is expected as the permeability values for site-3 are higher as compared to other two sites.

Table 10. Values of pore pressure applied at the interface

Point	Elevation below ground level (in ft)	Pore water pressure (in psf)
A	-29	62.4 x 29 = 1809.6
B	-44	62.4 x 44 = 2745.6

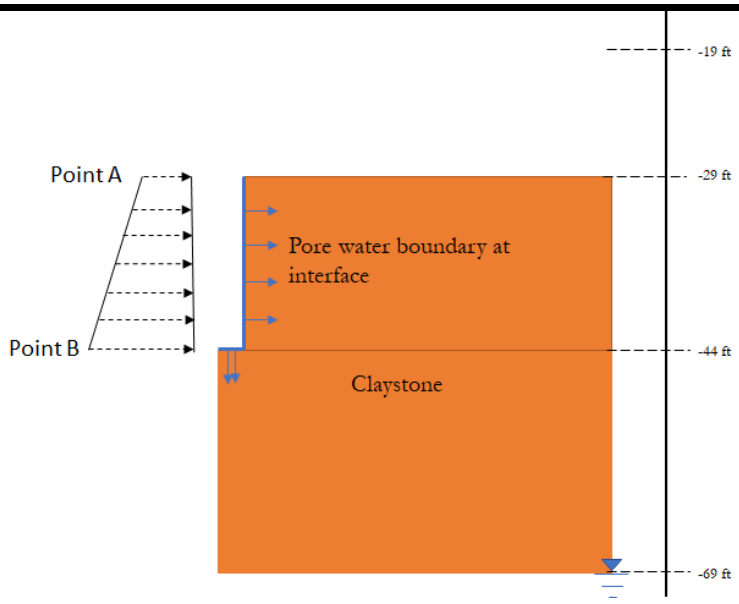

Figure 23. Pore pressure boundary applied at the interface

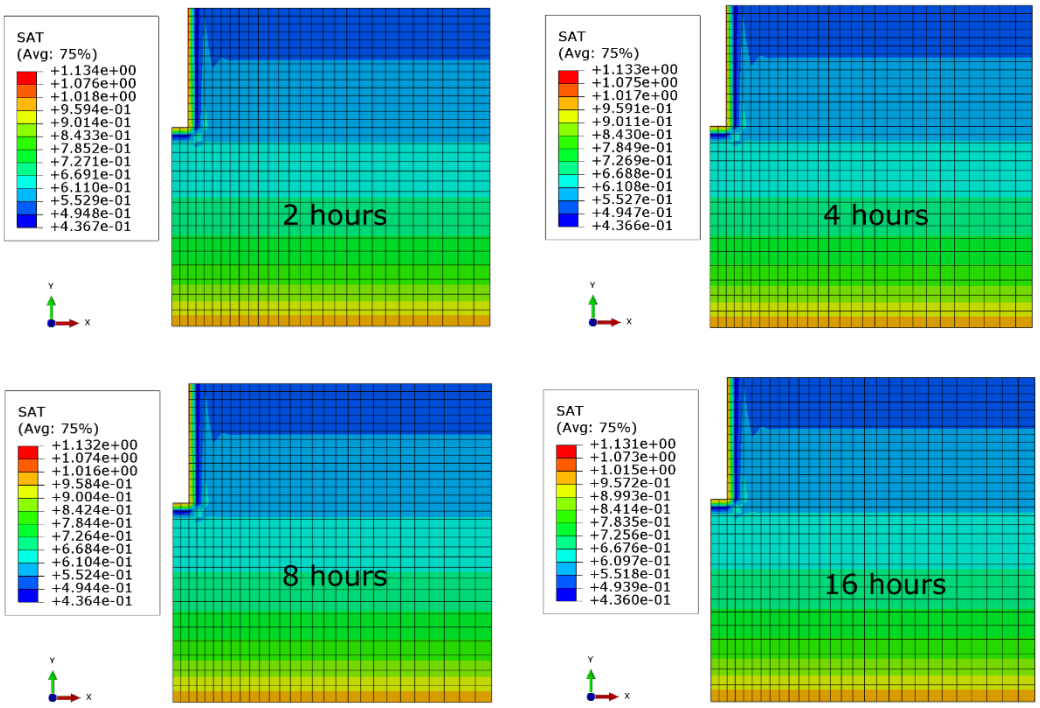

Figure 24. Saturation contours for site-1 at the end of wetting step for different wetting time values.

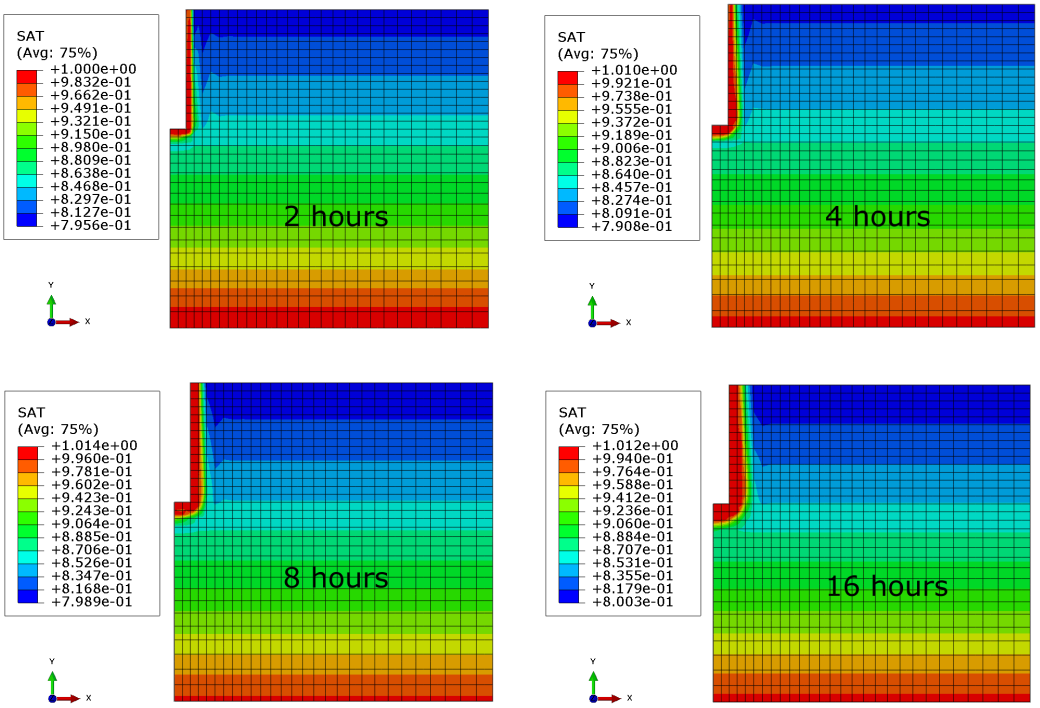

Figure 25. Saturation contours for site-2 at the end of wetting step for different wetting time values.

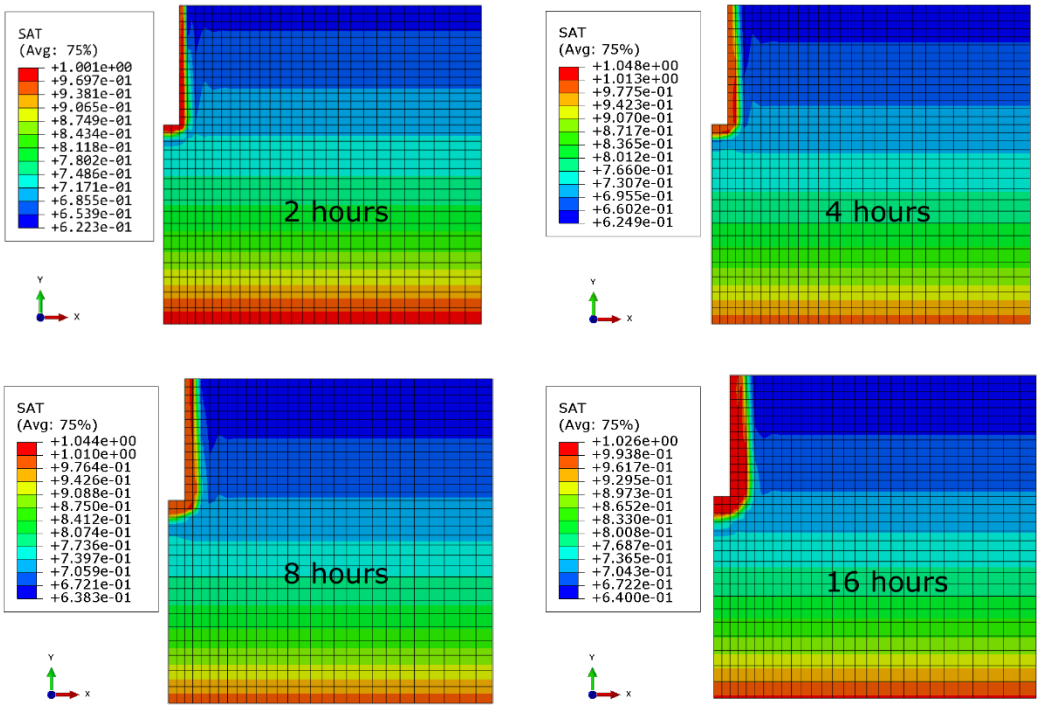

Figure 26. Saturation contours for site-3 at the end of wetting step for different wetting time values.

Figure 27, Figure 28 and Figure 29 show the degree of saturation as a function of the horizontal and vertical distances from the interface (where pore pressure boundary has been applied) for different wetting time for site-1, site-2 and site-3 respectively. The variation of the degree of saturation with vertical and horizontal distance are plotted, starting from the edge of the pile shaft at an elevation of 43 ft below the ground level. It is evident from these figures that there exists a considerable difference between the degree of saturation for different wetting time for site-3 and site-2. As far as site-1 is concerned, there exists no difference in the wetting profile for different wetting times due to its low permeability value. The zig-zag shape of the curves in in Figure 27 to Figure 29 is due to the coarse mesh and lack of resolved data points.

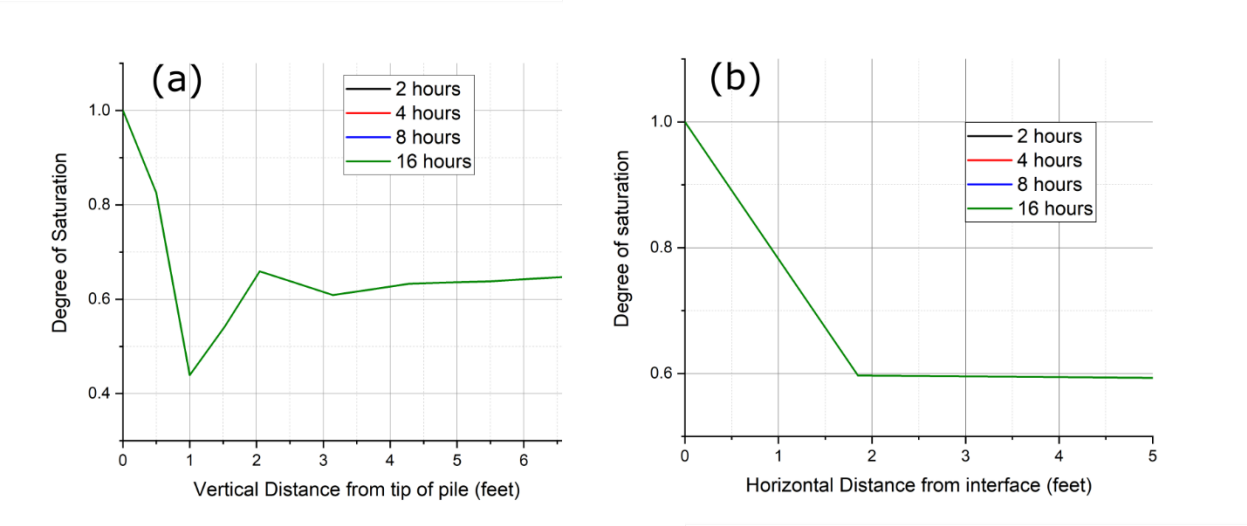

Figure 27. Spatial variation of degree of saturation near the pile face for site-1; (a) in vertical direction, (b) in horizontal direction.

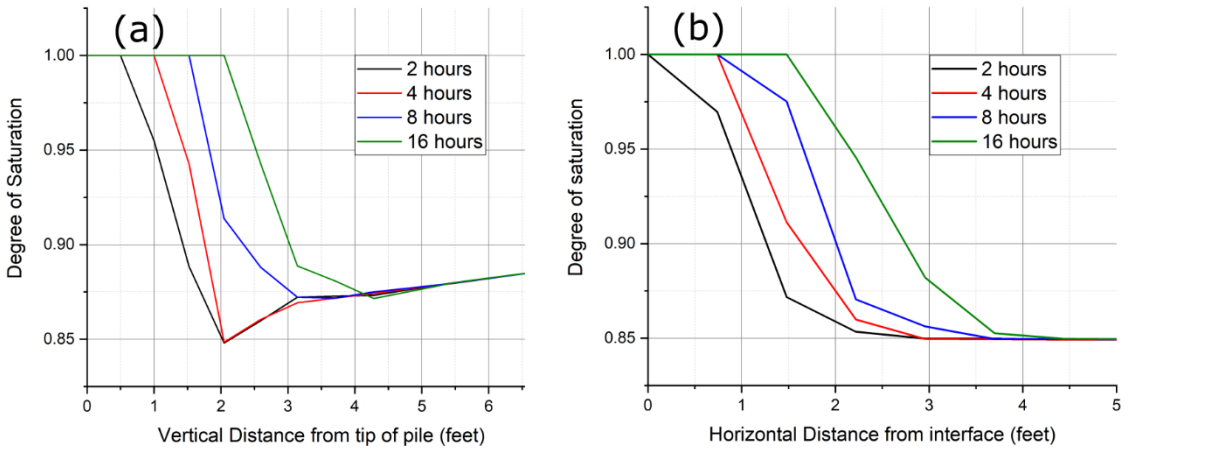

Figure 28. Spatial variation of degree of saturation near the pile face for site-2; (a) in vertical direction, (b) in horizontal direction.

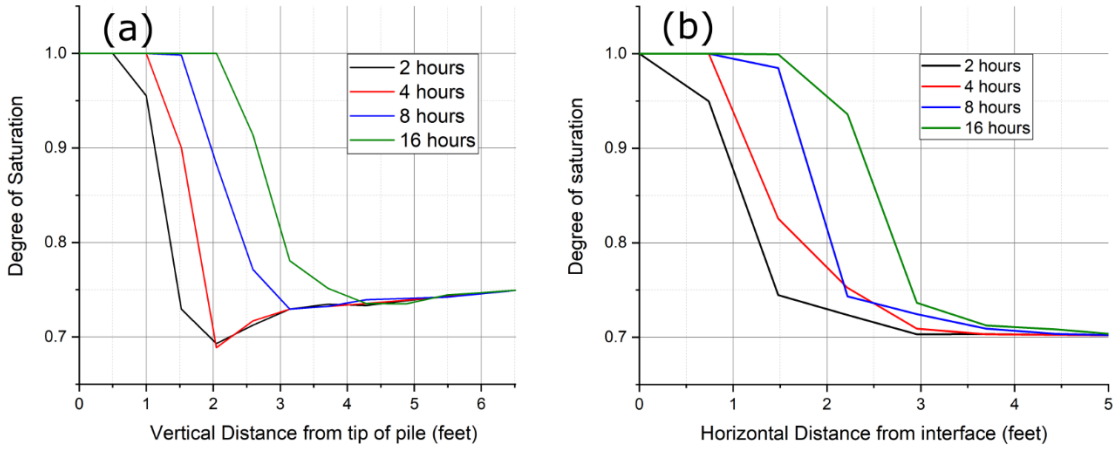

Figure 29. Spatial variation of degree of saturation near the pile face for site-3; (a) in vertical direction, (b) in horizontal direction.

3.4.3 Pile activation

This step simulates the placement of concrete in the borehole. At this step, the pile element is activated instantly but its gravity load is gradually applied in a linear manner. The lateral boundary condition supporting the claystone used to constrain the lateral movement of the borehole is removed in this step. This step lasts for 0.5 hours until the full gravity load is achieved. During this process, the equivalent overburden pressure applied at the bottom of the borehole is gradually removed to prevent heaving of the bottom as well as to mimic the gradual displacement of drilling fluid by the concrete.

As mentioned in section 3.1, the current model only simulates the lower part of the pile socketed in the claystone. The pile segments from ground surface to -19ft is omitted and converted to an equivalent pressure of 2850 psf. During this step, this pressure is linearly applied on the top of the pile in the model over the 0.5-hour time span.

The interface properties between the claystone and the pile are decided using the recommendations provided in Abaqus Manual 2016. The pile and the claystone surfaces are taken as the master and slave surfaces, respectively, because of the higher stiffness of concrete than claystone. The normal behavior of this interface is taken as hard contact with a nonlinear variation of overclosure and contact pressure to prevent the excessive penetration of the master nodes into the slave element.

During this step, the interface between the claystone and the pile is assigned as frictionless since the concrete is considered still wet.

3.4.4 Friction activation and pile axial loading step

Friction activation simulates the hardening of concrete paste into solid form. In this step, friction is activated at the interface between pile and bedrock. The only difference between this step and the previous step is, the tangential behavior is assigned as frictional with the coefficient of friction being 0.6. After the change of interface properties, a total of two hours is allowed to let the pile settle down and equilibrate with the geostatic stress field before the axial load test.

In the final step, axial load is applied via a uniformly distributed pressure on the top of the pile. The pressure linearly increases with time in a total of two-hour time span. The corresponding load-displacement data is then collected at the top of the pile for calculating its ultimate bearing capacity.

4. USER DEFINED FIELD (USDFLD)

The user defined field (USDFLD) is a user subroutine that allows the user to define field variables at a material point as a function of time or any other material point quantities. It can be used to introduce the solution-dependent material properties. The purpose of using the USDFLD in this analysis is to update the strength parameters with respect to changing degree of saturations at local material points. The equations used for updating strength parameters in this analysis are discussed in section 4.1 and the workflow of USDFLD is explained in section 4.2.

4.1 Equations for strength parameters

The equations that govern the variation of the apparent cohesion (c_p) and friction angle (ϕ_p) with respect to the degree of saturation have been determined by the direct shear tests as described in section 2.4.4 These values are computed based on total stresses and thus they are total strength parameters. However, as mentioned earlier in section 3.4.1, ABAQUS relies on effective stresses to calculate the deformation and failure of porous materials and thus require the effective strength parameters as the input for the Mohr-Coulomb model. Therefore, we need to first convert the total strength parameters to effective cohesion (c') and effective friction angle (ϕ') respectively.

For axis symmetric conditions, the Mohr-Coulomb criterion given by equation (3) and equation (9) can be expressed in invariant form as following. Here, equation (13) is the invariant form of

the Mohr-Coulomb failure criterion in terms of total stress and equation (14) is the invariant form of the Mohr-Coulomb failure criterion in terms of effective stress.

$$6\,p\,sin\phi_p - q\left(3 - sin\phi_p\right) + 6c_p\,cos\phi_p = 0 \tag{13}$$

$$6\,p'\,sin\phi' - q(3 - sin\phi') + 6c'\,cos\phi' = 0 \tag{14}$$

Where, p is the mean total stress, p' is the mean effective stress, q is the deviatoric stress that is same for effective and total stress, c_p is the peak apparent cohesion, $\phi_p$is the peak apparent friction angle, $c'$is the effective cohesion and ϕ' is the effective friction angle. Using the effective stress definition (12), the relationship between p and p' can be expressed as following:

$$p = p' - S\psi \tag{15}$$

Substituting p from equation (15) into equation (13) and rearranging, we get

$$6\,p'\,sin\phi_p - q\left(3 - sin\phi_p\right) + 6\left(c_p - S\psi\,tan\phi_p\right)cos\phi_p = 0 \tag{16}$$

Comparing equation (14) and equation (16), the following relationships between the total and effective strength parameters are obtained

$$\phi' = \phi_p \tag{17}$$

$$c' = c_p - S\psi\,tan\phi_p \tag{18}$$

The variation of total stress parameters φ_p and c_p with respect to suction pressure ψ are determined through experiments and collected in equations (5) and (7) respectively. These equations along with equations (17) and (18) are written in USDFLD to calculate the stress parameters at all the integration points in the analysis after extracting the values of saturation (or suction) at those points.

4.2 Workflow of USDLFD

The developed USDFLD collects the saturation and pressure values at every material point and then computes the strength parameters accordingly. Figure 30 shows the flow chart depicting the working of the user defined field in the analysis.

Initially, the saturation and suction values are extracted for all the material points and are stored as State Variable (1) and State Variable (2). Then the corresponding values of effective friction and cohesion are calculated at all the material points by using the strength equations provided in section 4.1 and are stored as Field variable (1) and Field Variable (2). Finally, in the finite element

model, the values of Field variable (1) and Field variable (2) are respectively passed to the effective friction angle and effective cohesion in a one-to-one manner to be used in the mechanical analysis. For visualization purpose, the Field Variable (1) and Field Variable (2) are also stored as State Variable (3) and State Variable (4), respectively. The USDFLD code is attached in the Appendix. The same code is used for different sites with the only difference being the parameters.

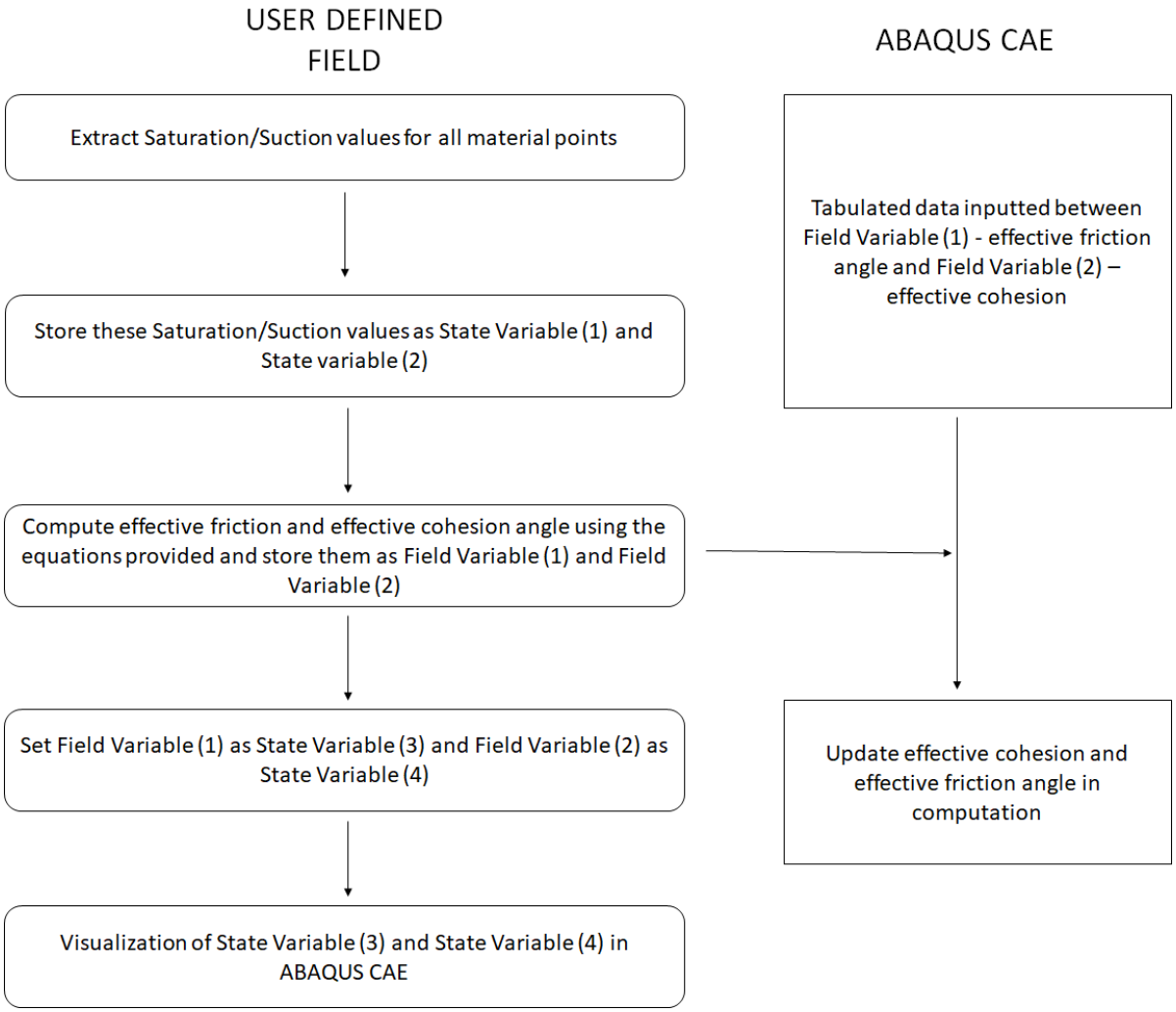

Figure 30. Working of User-Defined Field

5. RESULTS AND DISCUSSION

A series of simulations have been conducted for all three sites with different wetting time values including no wetting (zero wetting time), 2 hours, 4 hours, 8 hours, and 16 hours. The degradation of the claystone due to fluid infiltration is successfully captured by the developed USDFLD and the load displacement curves for all three sites are generated for the mentioned wetting time values. The ultimate axial load capacities are determined from the load displacement curves by using the Davisson's criterion. The simulation results for each site are discussed separately in this section followed by a comparison of the results for the three sites.

5.1 Simulation results for Site-1

The contours of effective cohesion at the end of wetting step for different wetting time, for site-1, are shown in Figure 31. As it seen for the figure, the difference of effective cohesion contours for different wetting time is negligible for site-1. This can be explained by examining Figure 24 and Figure 27. Both the figures show that the variation of the degree of saturation in the bedrock for different wetting time values is negligible for site-1. Therefore, though site-1 shows significant variation in the total strength parameters with respect the degree of saturation, this does not affect the effective cohesion distribution in the modeled rock mass much. As a result, the load displacement curve for different wetting time are almost identical for site 1 as shown in Figure 32. Therefore, the ultimate axial load capacity obtained using Davisson's method is also not affected by the wetting time for site-1.

5.2 Simulation results for site-2

Figure 33 shows the contours of effective cohesion at the end of wetting step for different wetting time for site-2. For site-2, there is a considerable difference in the cohesion contours for different wetting time. Specially, the zone of high degradation is near the pile face keeps getting larger with increasing wetting time. The degradation of rock mass results for the combined effect of total strength parameters with increasing degree of saturation (Figure 12) and the propagation of saturation front near the pile face with increasing wetting time (Figure 25).

The load displacement curves of pile in site-2 for different wetting time along with the Davisson's line are shown in Figure 34. It is observed that the load displacement curve becomes less stiff for increasing wetting time due to higher rock mass degradation. Therefore, the ultimate axial load capacity for pile in site-2 decreases considerably with increasing wetting time.

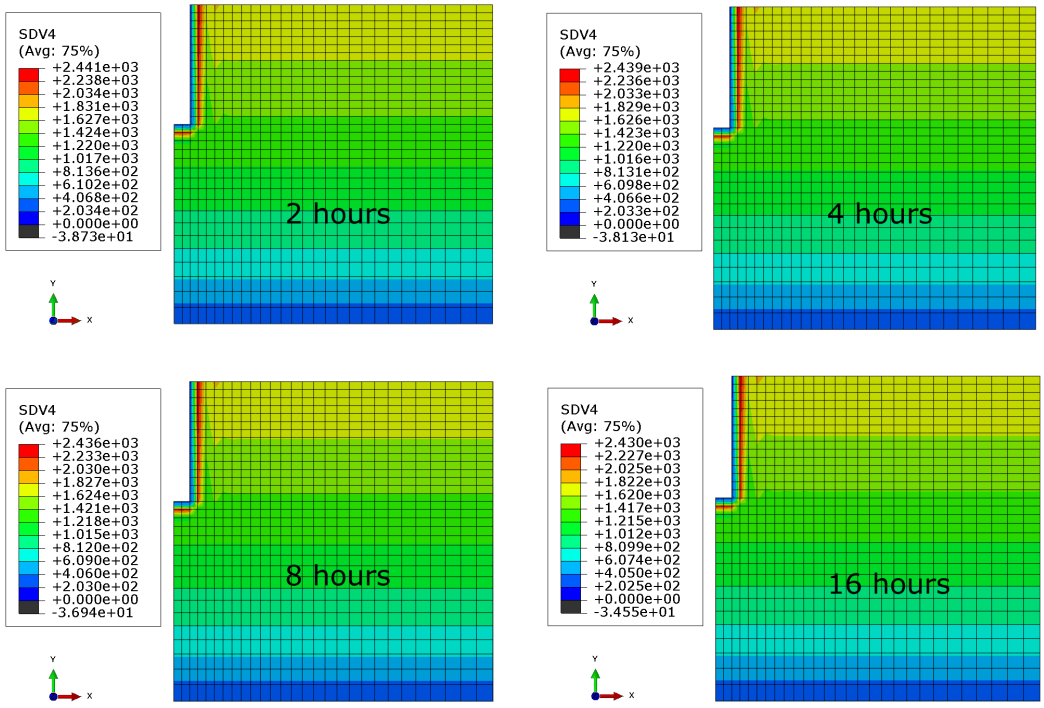

Figure 31. Cohesion contours for different wetting time values for site-1.

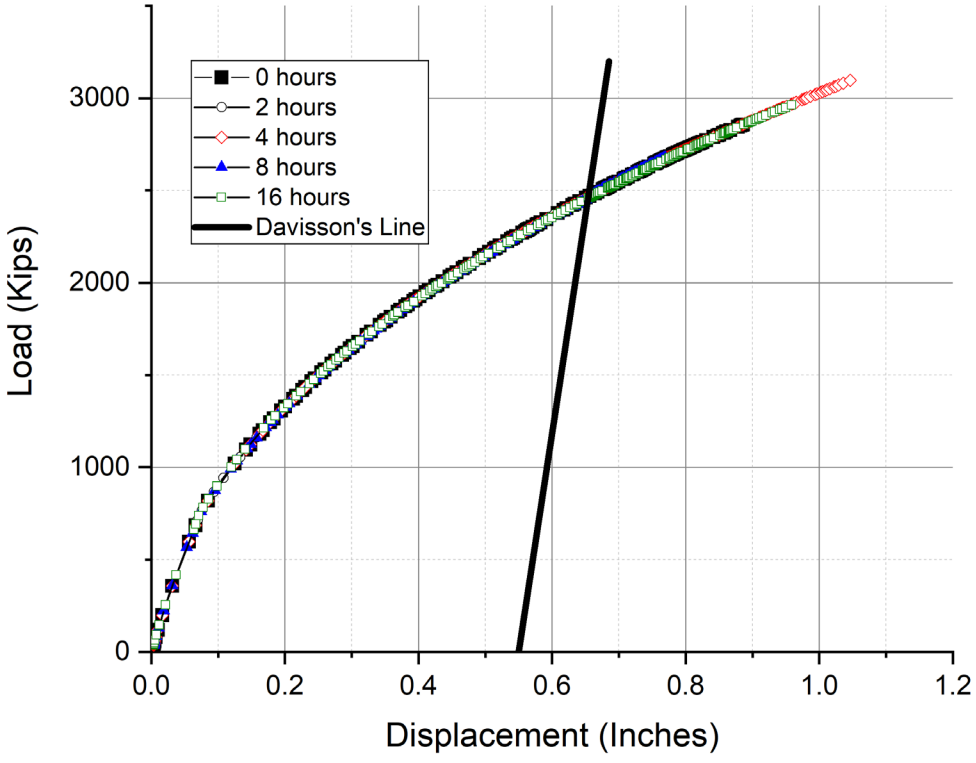

Figure 32. Load Displacement curve for site-1 for different wetting time values.

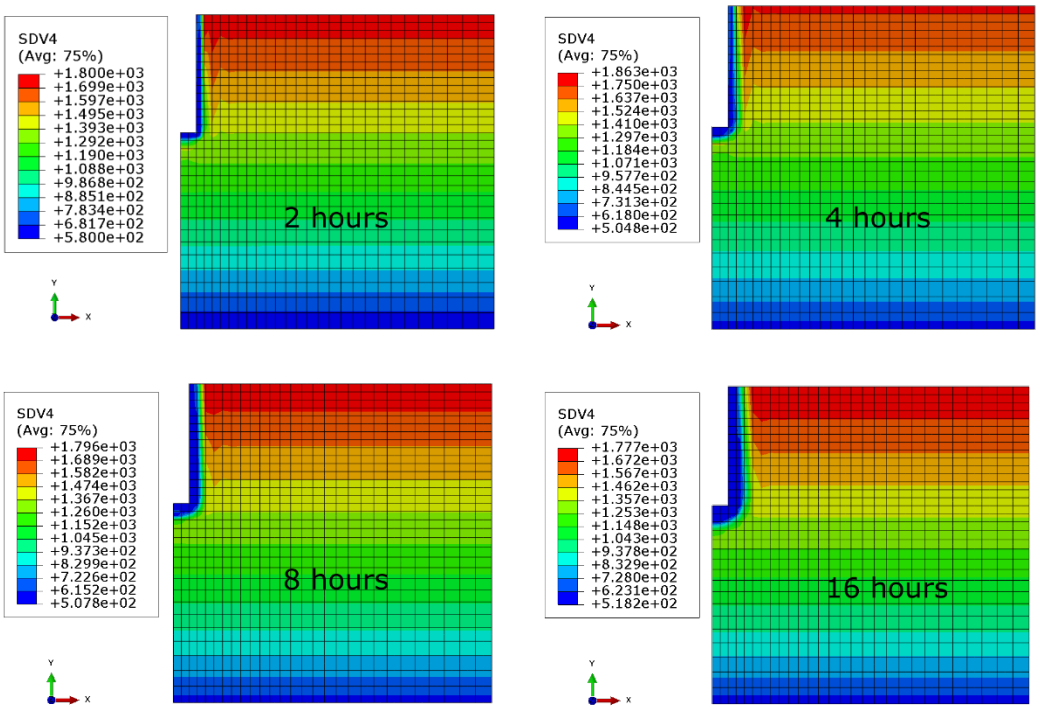

Figure 33. Cohesion contours for different wetting time values for site-2.

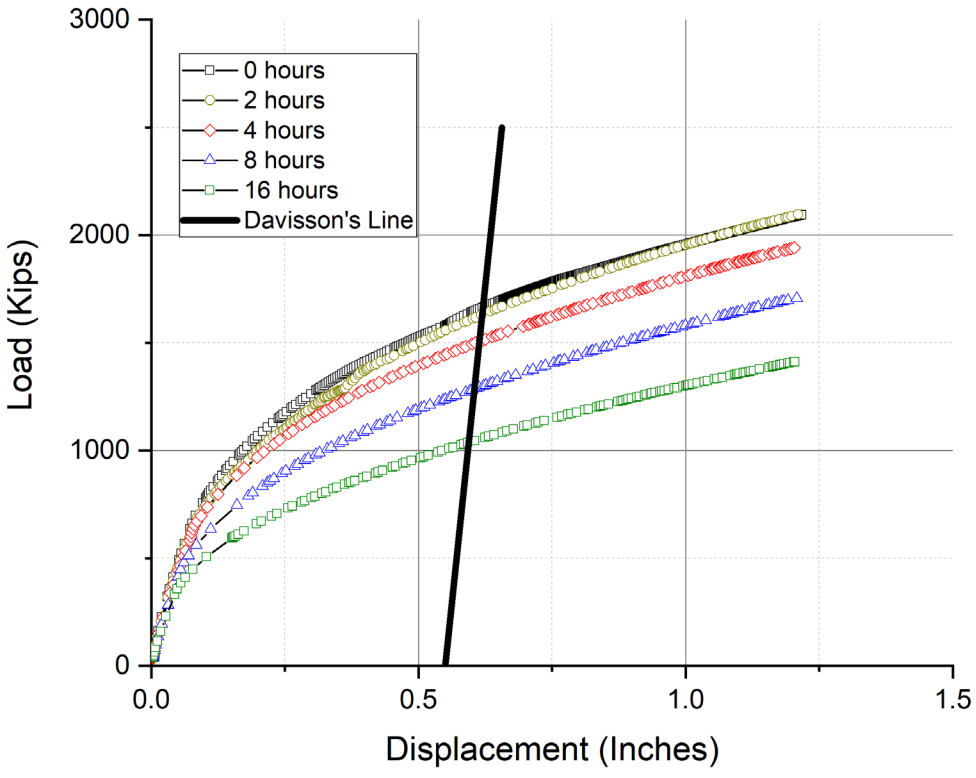

Figure 34. Load Displacement curve for site-2 for different wetting time values.

5.3 Simulation results for site-3

The contours of effective cohesion at the end of wetting step for different wetting time, for site-3, are shown in Figure 35. Considerable difference in the effective cohesion contours for different wetting time for site-3 is observed as well. Both the all over degradation of the rock mass and the extent of highly degraded zone near the pile face increases with increasing wetting time. This results in decreasing ultimate axial load capacity and less stiff load displacement curve with increasing wetting time for site-3 as shown in Figure 35. In addition, by comparing Figure 34 and Figure 36 it can be seen that the ultimate load bearing capacity of site-3 is more sensitive to the wetting time than site-2.

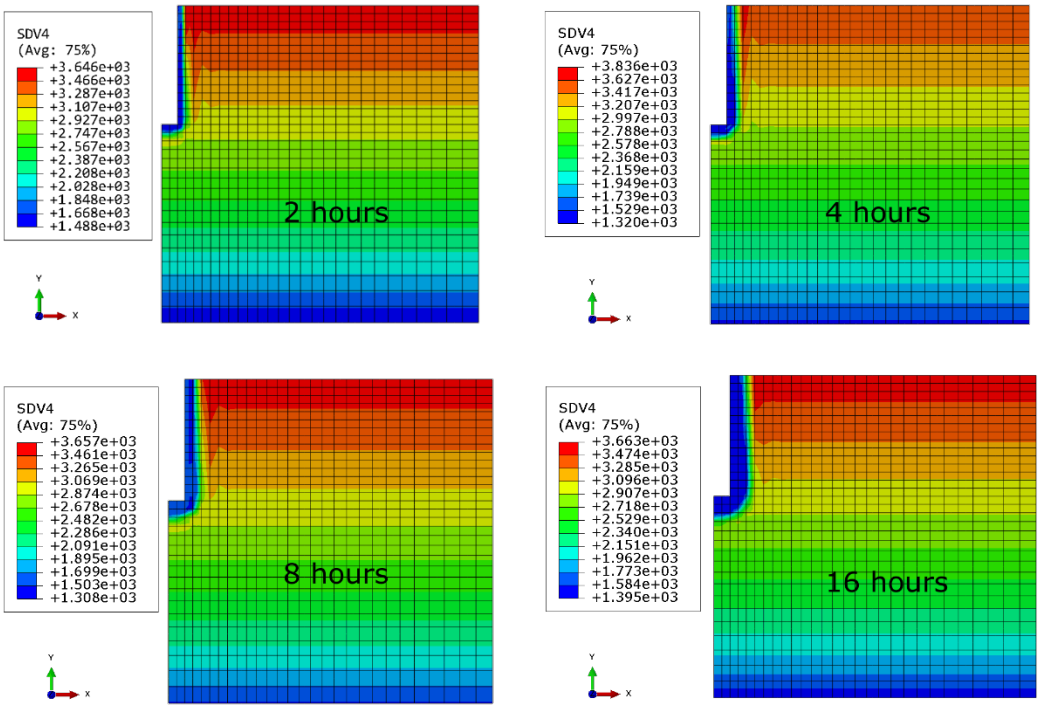

Figure 35. Cohesion contours for different wetting time values for site-3.

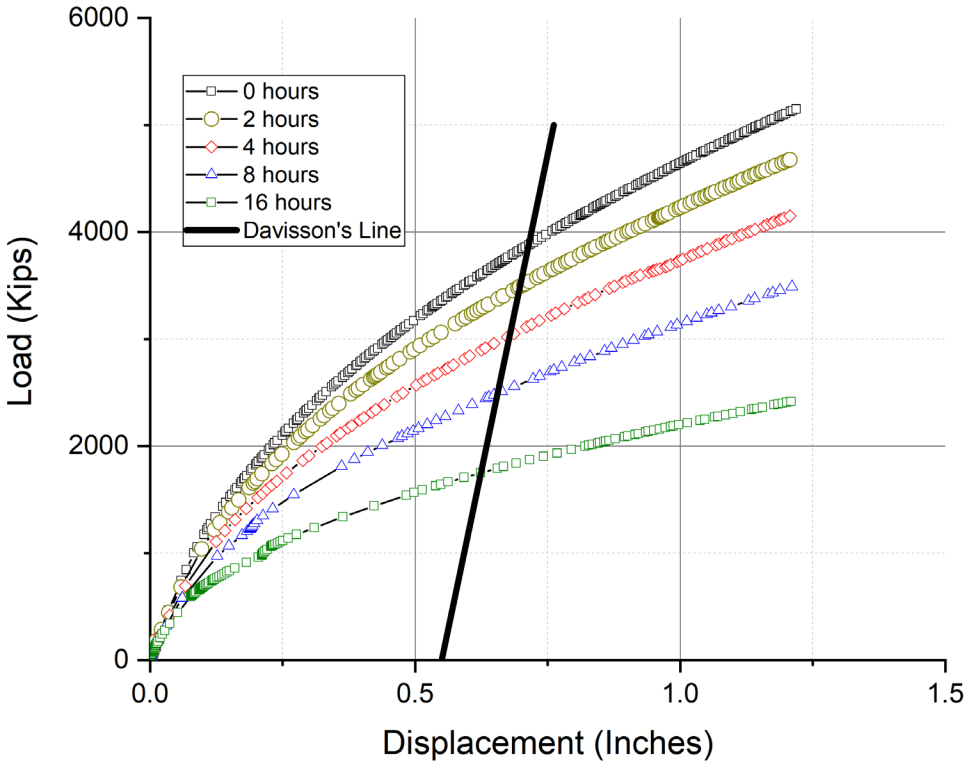

Figure 36. Load Displacement curve for site-3 for different wetting time values.

5.4 Comparison of the three sites

The variation of ultimate axial load capacity with wetting time for all three sites is plotted in Figure 37. As discussed before, the ultimate axial bearing capacity is not affected by the wetting time for site-1 because of the little variation in the saturation contours for different wetting time value. Significant reduction in the ultimate axial bearing capacity with increasing wetting time for site-2 and stie-3 is observed due to the formation of bigger zones of fully saturated rock mass near the pile face for higher values of wetting time.

The percentage reduction in the ultimate axial bearing capacity for different wetting time for the three sites is listed in Table 11. The ultimate axial bearing without wetting is taken as the reference value to compute the percentage reduction. It is also evident from Table 11 that site-3 is more sensitive to wetting for lower duration of wetting in comparison to site-2.

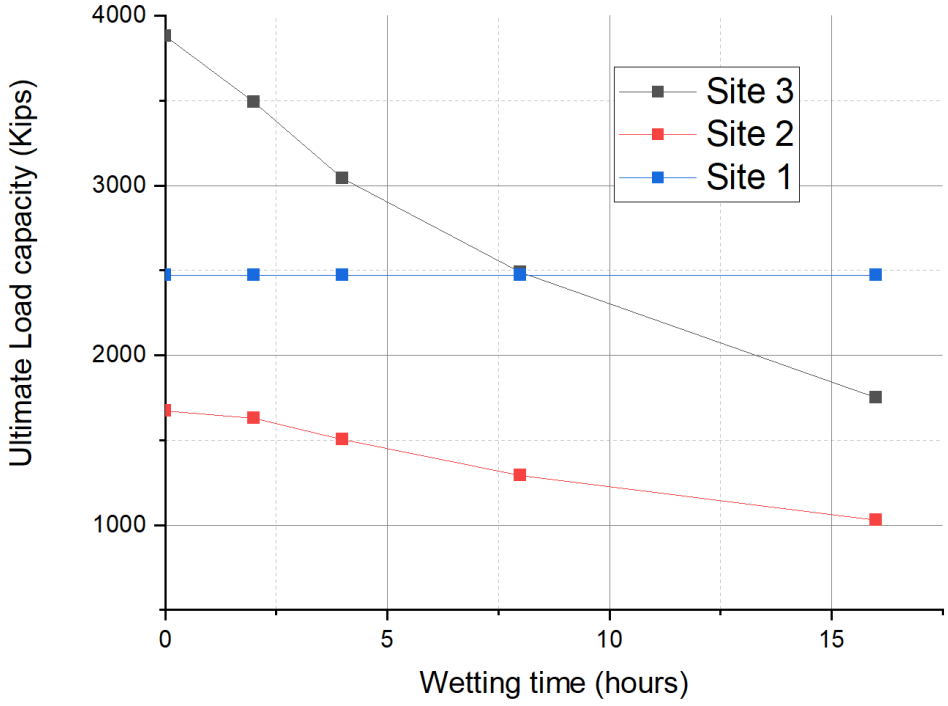

Figure 37. Variation in Ultimate axial load capacity with increasing wetting time for all three sites.

Table 11. Percentage reduction in the Ultimate axial load capacity for all three sites.

Wetting time (in hours)	Reduction in Ultimate Load Capacity		
	Site-1 (%)	Site-2 (%)	Site-3 (%)
0	Taking as the reference pile capacity		
2	0	2.46	10.05
4	0	9.88	21.65
8	0	22.75	35.82
16	0	38.32	54.90

The rock mass at the all three sites shows considerable variation in the total strength parameters with respect to the degree of saturation, but the sites with higher variation in the degree of saturation contours for different wetting time also show higher variation in the ultimate axial load caring capacity for different wetting time. From this it can be inferred that for the three sites tested in this study, the hydraulic properties of the rock mass are the major factors in determining the

sensitivity of axial load capacity to the wetting time. Site-1 with very low saturated hydraulic conductivity (7.12E-10 ft\sec) shows negligible sensitivity to wetting time, site-2 with higher saturated hydraulic conductivity (8.01E-08 ft\sec) shows considerable sensitivity and site-3 with highest saturated hydraulic conductivity (1.88E-07 ft\sec) exhibits the highest sensitivity to the wetting time. This indicates that the saturated hydraulic conductivity is the major factor governing the sensitivity of the ultimate axial load capacity with respect to the wetting time. To further verify this observation and detect other influencing factors, a parametric study is performed and presented in the next section.

6. PARAMETRIC STUDY

Considering the results obtained in section 5, a parametric study is conducted to quantify the effect of saturated hydraulic conductivity on the rate of degradation of the ultimate axial load capacity. In addition, we also varied the in-situ ground water table depth to learn the impact of initial saturation of the claystone on the capacity degradation, considering the location of the ground water table is likely to vary seasonally for a given site location. To perform the parametric study, all the model parameters and simulations steps described section 5 are used. All the material parameters are fixed to that of the site-3. Two sets of parametric studies are performed, with one only varying the saturated hydraulic conductivity and the other only varying the depth of the in-situ water table.

6.1 Effect of saturated hydraulic conductivity

Simulations for wetting time ranging from no wetting (zero wetting time) to 64 hours of wetting are conducted for three different values of saturated hydraulic conductivity. The variation of ultimate axial load capacity with wetting time for different saturated hydraulic conductivities is plotted in Figure 38 . Each data point is a result of one simulation of the full pile construction and axial loading process. It can be seen that the ultimate axial capacity for zero wetting time is the same of all the curve irrespective of the saturated hydraulic conductivity. For a given wetting time, higher saturated hydraulic conductivity results in lower ultimate axial capacity. It can also be seen that for higher saturated hydraulic conductivity the ultimate axial capacity decreases more rapidly. For very high wetting time, the influence of the saturated hydraulic conductivity on the ultimate axial load capacity becomes smaller because the spatial variation of the degree of saturation tends towards the equilibrium (or steady-state) distribution.

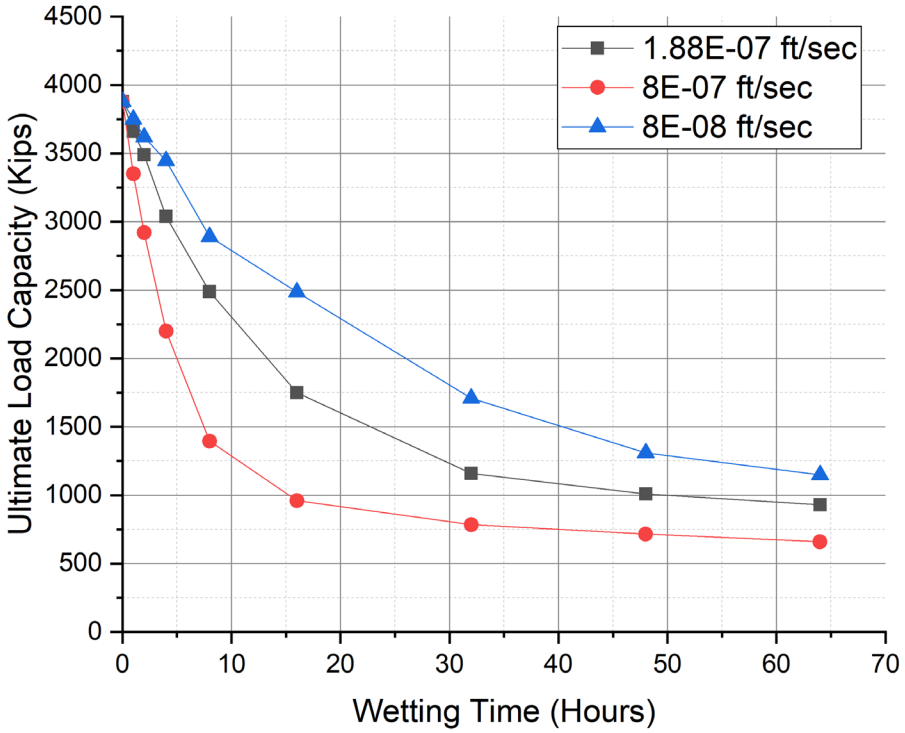

Figure 38. Effect of saturated hydraulic conductivity on variation of ultimate axial load capacity with wetting time.

6.2 Effect of in-situ water table location

Simulations for three different depths of the water table have been conducted. For each depth of water table, simulations with wetting time ranging from 0 to 64 hours are conducted. The variation of ultimate axial load capacity with wetting time for different depths of in-situ water table is plotted in Figure 39. There is significant difference between the ultimate axial load capacities at zero wetting time for different depths of water table. This is because the location of in-situ water table governs the spatial distribution of the degree of saturation prior to the wetting. For higher water table, the overall degree of saturation is also higher in the rock mass resulting in lower shear strength and hence lower ultimate axial load capacity. For a given wetting time, the ultimate axial load capacity is lower when the in-situ water table is higher. This difference is more pronounced for lower wetting time and becomes less pronounced for higher values of wetting time.

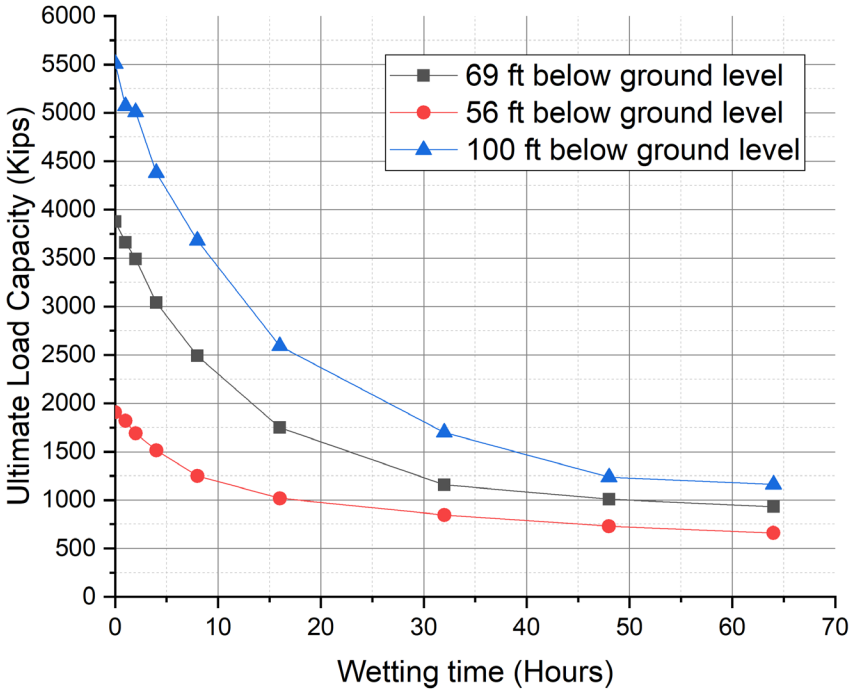

Figure 39. Effect of in-situ water table location on variation of ultimate axial load capacity with wetting time.

To highlight the relative loss in the ultimate axial load capacity with wetting time for different depths of the in-situ water table, normalized ultimate axial load capacity is plotted in Figure 40. For each depth of the water table, the ultimate axial load capacity at zero wetting time is taken as the reference value to normalize the ultimate axial load capacity at all the other values of the wetting time. It is observed that the relative loss of ultimate axial load capacity for lower values of wetting time is almost same for different depths of water table. For higher values of wetting time, the shallower water table results in less relative degradation in the ultimate axial load capacity as compared to the deeper ones. This observation indicates that the initial degree of saturation of the rock mass plays an important role in determining the sensitivity of pile capacity with respect t the wetting time. The more saturated the in-situ rock is, the less impact the wetting will cause on the axial capacity of the caisson.

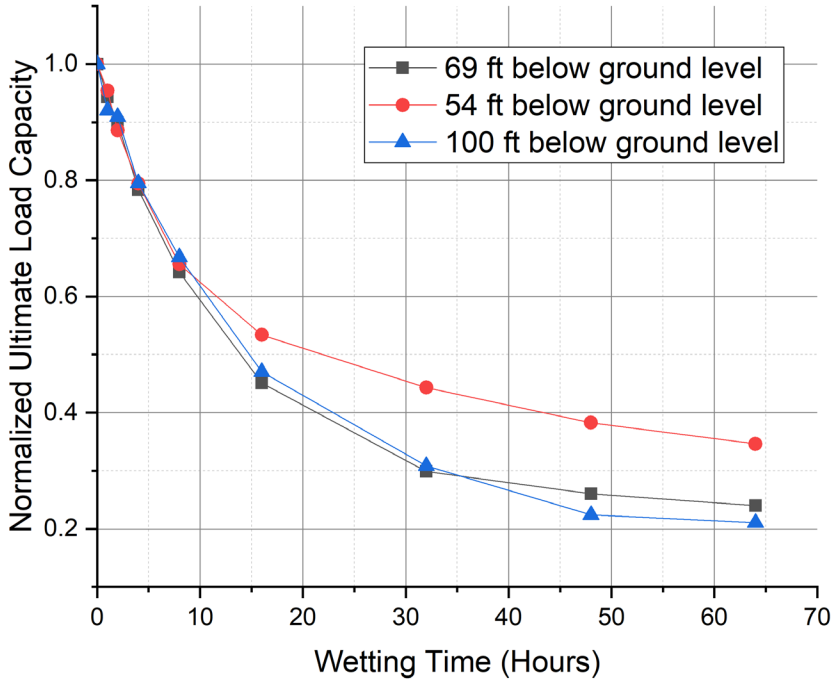

Figure 40. Reduction in normalized ultimate axial load capacity with increasing wetting time for different depths of in-situ water table.

7. CONCLUSIONS

In all three sites with various permeability and strength reduction characteristics simulated in section 5, the pile capacity reduction for four-hour wetting time compared is less than 22%. It is believed that this number is on the conservative side because of the following: 1) the direct shear test is conducted parallel to the bedding plane, which is the weakest direction of the rock and is believed to have the highest sensitivity to wetting; 2) water is used in the strength reduction tests to partially saturate the samples, which likely gives more slaking and degradation of the claystone than other drilling fluid (Hemphill et al., 2008; Karakul, 2018); 3) the pile hardening time is unrealistically short (two hours) and no time is given between the completion of pile and the pile load test, thus the moisture near the pile has little time to re-equilibrate with the adjacent rocks, giving the most undesirable scenario on about the ultimate axial capacity. **For above reasons, it is believed that the four-hour limitation is reasonable and perhaps on the conservative side of the construction of drilled caissons.** The parametric study performed in section 6 suggests that

the reduction in the ultimate axial load capacity with increasing wetting time is highly sensitive to the saturated hydraulic conductivity of the rock mass. The ultimate axial load capacity may decrease very quickly on wetting for relatively dry rock mass with very high saturated hydraulic conductivity. **Hence, for dry, highly weathered or fissured claystone with a permeability greater than the order of 10^{-8} ft/sec, a further deduction of the allowable wetting time would be justifiable to avoid excessive wetting and weakening of the rock matrix**.

Quantitative evaluation of whether the four-hour limitation can be relaxed to a longer duration requires more detailed study. For example, it will be useful to determine not only the degradation but also "the recovery of wetting" phase of the rock and relate them to the additional characteristics of the rock since there may be weeks before a load test is done after the construction of the pile. Different types of drilling fluids should also be done using the proposed procedure and incorporated in the numerical study. Upon CODT's specification of an acceptable bearing capacity reduction, an allowable wetting time for a particular project can be more reliably determined. With more experimental data gathered by the procedure developed in this study, to the development of a design chart for the allowable wetting time, with the slaking index and permeability as two input parameters is believed to be possible and recommended for local foundation practice

REFERENCES

ABAQUS. 2016. *ABAQUS Documentation*. Providence, RI, USA: Dassault Systems.

Abu-hejleh, Naser, and William J. Attwooll. 2005. "Colorado's Axial Load Tests on Drilled Shafts Socketed in Weak Rocks: Synthesis and Future Needs."

Abu-Hejleh, Naser, Michael O'Neill, Dennis Hanneman, and William Attwooll. 2005. "Improvement of the Geotechnical Axial Design Methodology for Colorado's Drilled Shafts Socketed in Weak Rocks." *Transportation Research Record* 1936: 100–107. https://doi.org/10.3141/1936-12.

Bäker, Martin. 2018. "How to Get Meaningful and Correct Results from Your Finite Element Model." *ArXiv Preprint ArXiv:1811.05753*, 1–26. http://arxiv.org/abs/1811.05753.

Claybourn, Alan F. 2007. "Failure of Drilled Piers in Denver Due to Formation of Softened Claystone." *Contemporary Issues In Deep Foundations*, 1–11. https://doi.org/10.1061/40902(221)22.

Coussy, Olivier, and Ulm Franz. 1995. "Mechanics of Porous Continua." *Chichester: Wiley* 1016.

Genuchten, M. T. Van. 1980. "A Closed-Form Equation for Predicting the Hydraulic Conductivity of Unsaturated Soils." *Soil Science Society of America Journal* 44.5: 892–98.

Hemphill, Terry, Younane N. Abousleiman, Minh Ha Tran, Son Hoang, and Vinh Nguyen. 2008. "Direct Strength Measurements of Shale Interaction with Drilling Fluids." In *Abu Dhabi International Petroleum Exhibition and Conference. Society of Petroleum Engineers.* https://doi.org/10.2118/117851-ms.

Karakul, Hasan. 2018. "Effects of Drilling Fluids on the Strength Properties of Clay-Bearing Rocks." *Arabian Journal of Geosciences* 11 (16). https://doi.org/10.1007/s12517-018-3816-8.

Lu, Ning, Murat Kaya, and Jonathan W. Godt. 2014. "Interrelations among the Soil-Water Retention, Hydraulic Conductivity, and Suction-Stress Characteristic Curves." *Journal of Geotechnical and Geoenvironmental Engineering* 140 (5): 04014007 (1-10). https://doi.org/10.1061/(asce)gt.1943-5606.0001085.

Pineda, J.A., E.E. Alonso, and E. Romero. 2013. "Environmental Degradation of Claystones." *Géotechnique* 64 (1): 64–82. https://doi.org/10.1680/geot.13.p.056.

Seo, Hoyoung, Monica Prezzi, and Rodrigo Salgado. 2008. "Settlement Analysis of Axially Loaded Piles." https://doi.org/10.1061/(asce)0733-9410(1991)117:11(1706).

Sheng, Daichao, K. Dieter Eigenbrod, and Peter Wriggers. 2005. "Finite Element Analysis of Pile Installation Using Large-Slip Frictional Contact." *Computers and Geotechnics* 32 (1): 17–26. https://doi.org/10.1016/j.compgeo.2004.10.004.

USGS.gov. n.d. "USGS Current Water Data for Colorado." https://waterdata.usgs.gov/co/nwis/rt.

Appendix A. FORTRAN Code for the USDFLD Subroutine

```
1
      C  User subroutine
2     C
3           SUBROUTINE USDFLD (FIELD, STATEV, PNEWDT, DIRECT, T, CELENT,
4          1 TIME, DTIME, CMNAME, ORNAME, NFIELD, NSTATV, NOEL, NPT, LAYER,
5          2 KSPT, KSTEP, KINC, NDI, NSHR, COORD, JMAC, JMATYP, MATLAYO,
6          3 LACCFLA)
7     C
8           INCLUDE 'ABA_PARAM.INC'
9     C
10          PARAMETER (PR=20.885D0, CO=1503.751D0, C2=245.194D0, AP=0.3107D0, PI=180.0D0/3.14)
11    C
12          CHARACTER*80 CMNAME, ORNAME
13          CHARACTER*8 FLGRAY (15)
14          DIMENSION FIELD(NFIELD), STATEV(NSTATV), DIRECT (3,3),
15         1 T (3,3), TIME (2)
16          DIMENSION ARRAY (15), JARRAY (15), JMAC (*), JMATYP (*),
17         1 COORD (*)
18    C
19    C User Code Start
20    C
21    C FIND THE SATURATION INFORMATION
22    C
23          CALL GETVRM ('SAT', ARRAY, JARRAY, FLGRAY, JRCD, JMAC, JMATYP, MATLAYO,
24         1 LACCFLA)
25    C
26     SAT=ARRAY (1)
27    C
28     STATEV (1) =SAT
29    C
30    C FIND THE PORE PRESSURE INFORMATION
31    C
32          CALL GETVRM ('POR', ARRAY, JARRAY, FLGRAY, JRCD, JMAC, JMATYP, MATLAYO,
33         1 LACCFLA)
34    C
35     POR=ARRAY (1)
36    C
37     STATEV (2) =POR
38    C
39    C POSITIVE PORE PRESSSURE
40    C
41     IF (STATEV (2) >= -PR) THEN
42     FIELD (1) =0
43    C
44     STATEV (3) =FIELD (1)
45    C
46          FIELD (2) =CO
47    C
48          STATEV (4) =FIELD (2)
49    C
50    C NEGATIVE PORE PRESSURE
51    C
52          ELSE
53     FIELD (1) =atand (AP*LOG10(-STATEV(2)/PR))
54    C
55     STATEV (3) =FIELD (1)
56    C
57     FIELD (2) =CO+C2*((LOG10(-STATEV(2)/PR))**2)-STATEV(1)*STATEV(2)*tand(STATEV(3))
58    C
59     STATEV (4) =FIELD (2)
60    C
61          ENDIF
62    C
63    C If error, write comment to .DAT file:
```

```
64          IF(JRCD.NE.0) THEN
65           WRITE (6, *) 'REQUEST ERROR IN USDFLD FOR ELEMENT NUMBER ',
66          1 NOEL,'INTEGRATION POINT NUMBER ', NPT
67          ENDIF
68      C
69          RETURN
70          END
```